SERI/TP-211-3666
DE90000319

March 1990

Characterization and Comparison of Optically Transparent Conducting Films

Final Subcontract Report
1 October 1988 - 30 November 1989

R. G. Gordon, Principal Investigator
Harvard University
Cambridge, Massachusetts

Prepared under Subcontract No. XX-8-18148-1

SERI

Solar Energy Research Institute
A Division of Midwest Research Institute

1617 Cole Boulevard
Golden, Colorado 80401

Operated for the
U.S. Department of Energy
under Contract No. DE-AC02-83CH10093

SERI/TP--211-3666

DE90 000319

SERI/TP-211-3666
UC Category: 270
DE90000319

Characterization and Comparison of Optically Transparent Conducting Films

Final Subcontract Report
1 October 1988 - 30 November 1989

R. G. Gordon, Principal Investigator
Harvard University
Cambridge, Massachusetts

March 1990

SERI Technical Monitor: W. Luft

Prepared under Subcontract No. XX-8-18148-1

Solar Energy Research Institute
A Division of Midwest Research Institute

1617 Cole Boulevard
Golden, Colorado 80401-3393

Prepared for the
U.S. Department of Energy
Contract No. DE-AC02-83CH10093

NOTICE

Printed in the United States of America
Available from:
National Technical Information Service
U.S. Department of Commerce
5285 Port Royal Road
Springfield, VA 22161

Price: Microfiche A01
Printed Copy A04

Codes are used for pricing all publications. The code is determined by the number of pages in the publication. Information pertaining to the pricing codes can be found in the current issue of the following publications which are generally available in most libraries: *Energy Research Abstracts (ERA)*; *Government Reports Announcements* and Index (*GRA* and I); *Scientific and Technical Abstract Reports (STAR)*; and publication NTIS-PR-360 available from NTIS at the above address.

SUMMARY

1.0 OBJECTIVES

Transparent conducting materials are essential components of thin-film solar cells, in which they serve as front-surface electrodes. In tandem cells, back surface electrodes also need to be transparent. Finally, some designs for highly reflective back contacts also call for a transparent conducting layer. The compositions of these transparent conducting layers are usually based on oxides of tin, indium and/or zinc, and are hence referred to as transparent conducting oxides (TCO). In addition to having low electrical resistance and low optical absorption, the structure of a TCO must minimize reflection losses. The TCO must also resist degradation during cell fabrication and use. Finally, the method for making the TCO must be inexpensive and safe.

Our general objectives are to improve the performance of TCO materials and the methods for their production. We aim to reduce their electrical resistance, optical absorption and reflection losses, and to avoid degradation of the materials. For the production method, the prime consideration is to deposit the TCO layers at a high rate with relatively simple apparatus.

The specific objectives of this research are to: 1) develop an ability to tailor the texturing of tin oxide (SnO_2) for optimum light trapping through a better understanding of the growth factors, crystal orientation, and early morphology (nucleation) of texturing; 2) develop state-of-the-art zinc oxide (ZnO) films through optimizing source materials, doping levels, and improving adhesion to substrates; 3) deposit and characterize the optical and electrical properties of SnO_2/ZnO hybrid films; and 4) deposit titanium nitride (TiN) films at substrate temperatures suitable for use as reflecting back contacts in a-Si:H p-i-n devices and characterize the optical and electrical properties of these films.

2.0 DISCUSSION

2.1 Textured Tin Oxide Films

The most commonly used TCO for thin-film solar cells is fluorine-doped tin oxide. In order to optimize the light-trapping efficiency of these films, we studied the effect of deposition conditions on the structure and properties of the films.

The fluorine doped tin oxide films were produced by atmospheric pressure chemical vapor deposition from dimethyltin dichloride, trifluorobromomethane, and oxygen. Very high growth rates, up to 50,000 angstroms per minute, were achieved. Electrical and optical properties of these films were measured for varying deposition temperatures and for varying Freon concentrations. Visible transmission as high as 85% and infrared reflection as high as 85% were obtained. Diffuse transmission measurements indicate that film roughness increases with increasing deposition temperature and with increasing oxygen concentration. The bulk conductivity of some films was over 2000 $\Omega^{-1}cm^{-1}$. Hall effect measurements gave mobilities from 12 to 36 $cm^2/V\text{-}s$ and electron concentrations of $1.0 - 4.2 \times 10^{20}$ cm^{-3}. The optical spectra were fit to an ionized-impurity scattering model that includes the effects of grain boundaries. This model was found to fit the data very well.

2.2 Discovery of Electrically Conductive Fluorine-doped Zinc Oxide

Zinc oxide is a promising material for forming less expensive TCO layers, since zinc metal is much less expensive than tin or indium. Also, zinc is much more abundant in the earth's crust, than is tin or indium, so that even large-scale use of solar cells would not lead to any shortage of zinc.

Also, zinc is widely distributed on earth, and is mined in many countries, so continuity of supply is assured in any kind of political situation. In contrast, tin is mined in large quantities in only a few countries. Another advantage of zinc oxide is its greater stability toward hydrogen plasmas used to deposit amorphous silicon solar cells.

As a preparation method, we chose chemical vapor deposition (CVD), since for many materials, the highest deposition rates have been achieved using CVD. When operated at atmospheric pressure, CVD requires only simple equipment which is commercially available and capable of large-area coating.

Pure zinc oxide has low electrical conductivity. By partial reduction, nonstoichiometric (oxygen-deficient) zinc oxide can be prepared with high electrical conductivity, which is, however, unstable. Group III elements (boron, aluminum or indium) have been added to zinc oxide to produce more stable, highly conductive films. However, out-diffusion of these group III dopants into amorphous silicon could produce uncontrolled doping of the amorphous silicon during deposition or use of the cell. We discovered that fluorine can also be used to dope zinc oxide to high electrical conductivity. Fluorine is an ideal dopant for zinc oxide, since it is known to be electrically inactive, or even beneficial, in hydrogenated amorphous silicon. An additional benefit of the fluorine doped zinc oxide is its higher electron mobility, which results in greater transparency.

The fluorine-doped zinc oxide is produced by CVD from diethyl zinc, ethanol and hexafluoropropylene at atmospheric pressure, in the temperature range 375° to 450°C. Films deposited under these conditions show good adhesion to the glass substrates (Scotch tape test). The highest electrical conductivity and light transmission are found for films deposited at the highest temperatures (450°C), and containing about 0.5 atomic percent fluorine. With this material, we could produce a TCO with a sheet resistance of 10 ohms per square and a visible transmission of about 80%. The films were too smooth to have high light-trapping efficiency.

2.3 SnO_2/ZnO Hybrid films

Hybrid tin oxide/zinc oxide films were successfully formed by successive CVD of textured fluorine-doped tin oxide and then smooth fluorine-doped zinc oxide. Amorphous silicon solar cells formed on these hybrid substrates at Chronar Corporation had higher efficiencies than those formed on the same batch of tin oxide without the extra zinc oxide layer. This hybrid combines the demonstrated good light-trapping of the tin oxide layer with the improved stability of the zinc oxide toward a hydrogen plasma during deposition of amorphous silicon.

2.4 TiN Reflecting Back Contacts

Titanium nitride is a metallic conductor with high reflectivity in the red and infrared parts of the spectrum. TiN has outstanding chemical and mechanical stability. It contains inexpensive and abundant elements. Thus TiN is a good candidate for forming durable and inexpensive back contacts to solar cells. It may also be used as a diffusion barrier between metals, such as aluminum or silver, and the amorphous silicon in a solar cell. We discovered a new process for low temperature synthesis of titanium nitride by CVD by reacting $Ti(NMe_2)_4$ and NH_3 vapors. TiN coatings containing less than one atom per cent of carbon and oxygen, were deposited at temperatures of about 200°C, which is low enough to use for deposition of back contacts on amorphous silicon solar cells. The films were analyzed by Rutherford backscattering spectrometry and X-ray photoelectron spectroscopy.

2.5 Optical Tuning of Front and Back Contacts

Optimization of deposition conditions for all these layers should be carried out with respect to the efficiency of solar cells made with the layers. So far, such optimization has only been carried out for the textured tin oxide layers, in collaboration with Chronar Corporation. Textured tin oxide films with a diffuse transmission for red light of about 5% proved to be optimum. Since our laboratory is not equipped with a full cell fabrication and testing facility, further optimization will require collaboration with other laboratories with these facilities.

3.0 CONCLUSIONS

- Textured tin oxide films with high light-trapping efficiency, high electrical conductivity and high transparency were successfully grown at high rates by chemical vapor deposition. This process has achieved large-scale commercial production of substrates for amorphous silicon solar cells.

- Highly transparent and highly conductive films of fluorine-doped zinc oxide were formed by a new CVD process. Increases in the texture (light-trapping) and growth rate are needed to make this a practical process for making substrates for solar cells. Decreases in deposition temperature are needed to make successful back contacts.

- A hybrid TCO consisting of textured tin oxide covered with a thin, smooth fluorine-doped zinc oxide layer combines the best features of these two materials. It shows efficient light-trapping because of the textured tin oxide, combined with the good resistance of zinc oxide to the hydrogen plasma used to deposit the amorphous silicon.

- Highly conductive and reflective titanium nitride was deposited under conditions mild enough to form back contacts on amorphous silicon solar cells. Actual cells will be coated and tested in the next contract period.

- Further optimization of the deposition conditions for these materials should be carried out in collaboration with solar cell manufacturers.

TABLE OF CONTENTS

LIST OF FIGURES

LIST OF TABLES

4.0 ELECTRICAL AND OPTICAL PROPERTIES OF CVD TIN OXIDE FILMS PREPARED BY THE OXIDATION OF DIMETHYLTIN DICHLORIDE

Abstract

Fluorine doped tin oxide films were produced by atmospheric pressure chemical vapor deposition from dimethyltin dichloride, trifluorobromomethane, and oxygen. Electrical and optical properties of these films were measured for varying deposition temperatures and for varying Freon concentrations. Visible transmission as high as 85% and infrared reflection as high as 85% were obtained. Hall effect measurements gave mobilities from 12 to 36 $cm^2/V\text{-}s$ and electron concentrations of $1.0 - 4.2 \times 10^{20}$ cm^{-3}. The optical data were fit to a grain boundary scattering model.

4.1 Introduction

Due to the unique properties of visible transparency, infrared reflectivity, electrical conductivity, and great durability, tin oxide thin films have been used as heat mirror coatings on glass and as front contacts for solar cells. Since these properties are primarily determined by the contributions of free electrons in the conduction band of the semiconductor, the mechanisms of conductivity, reflectivity and transparency are interdependent. Optimization of these materials for a specific application involves a trade-off between these different concerns.

The free electrons modify the spectral film properties in a characteristic way, as shown in Figure 1. In the visible range the spectral transmission shows the high values typical of normal dielectrics, modified by interference effects. In the near infrared, however, the transmission shows a marked decrease and the reflection increases to very high values, comparable to those of a metal. The crossover point between the two types of behavior is determined by the plasma oscillation of the free electrons and hence is referred to as the plasma wavelength. With increasing free-electron density, the plasma wavelength shifts to shorter wavelengths.

In this section, materials properties of fluorine doped tin oxide films produced by atmospheric pressure chemical vapor deposition (APCVD) from dimethyltin dichloride (DMTC), bromotrifluoromethane (Freon 13B-1), and oxygen will be presented. A coherent model relating the electrical and optical properties will be summarized. The material will be shown to have good electrical properties as illustrated by a high DC conductivity and high Hall mobility, as well as good optical properties, as illustrated by high visible transmittance and high infrared reflectance. Surface roughness can have a dramatic influence on the material properties. In photovoltaic devices, surface roughness enhances light trapping, thus improving cell performance. In heat mirror coatings, surface roughness leads to undesirable haze. The material will be shown to have a range of surface roughnesses depending on deposition conditions.

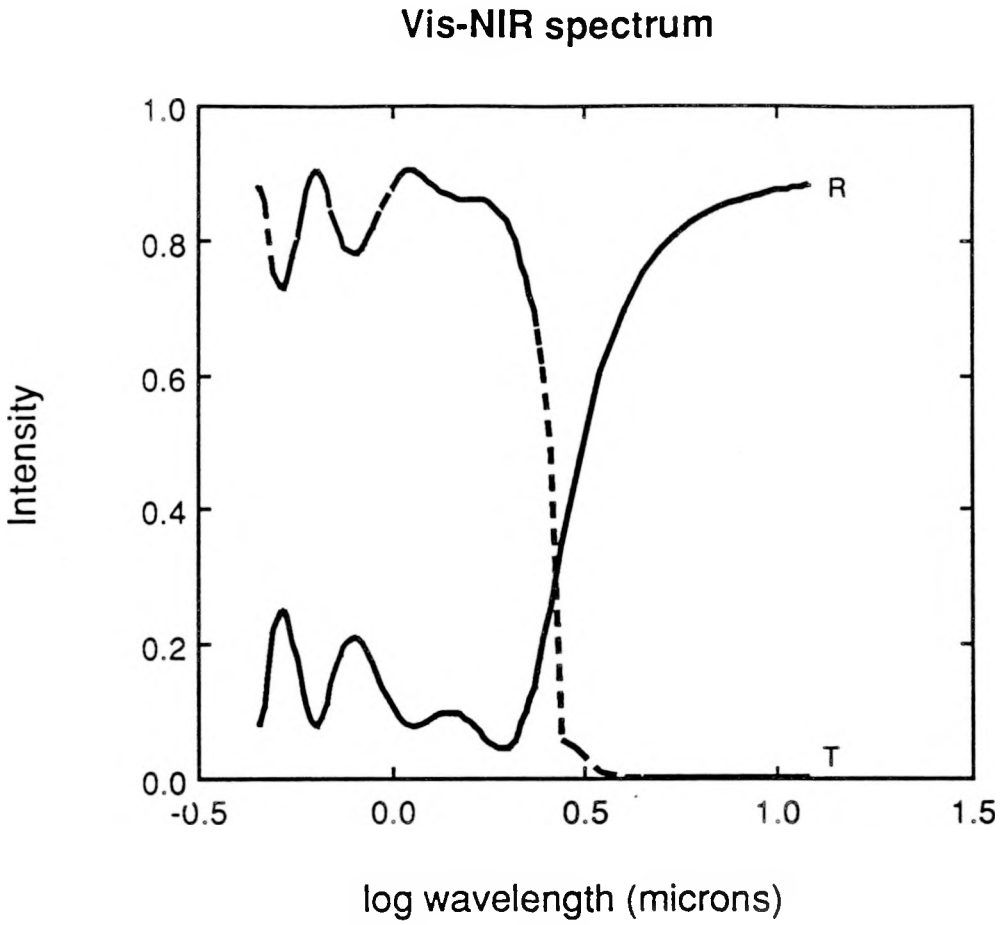

Figure 1. Typical Visible-Near Infrared for 0.3 micron thick, fluorine-doped tin oxide thin film.

4.2 Experimental

Fluorine doped tin oxide films were deposited from DMTC, Freon 13B-1 (CF_3Br), and oxygen in a cold wall, laminar flow APCVD reactor. The reactor is shown schematically in cross-section in Figure 2. The gas mixture enters the heated reactor through a row of small, closely spaced holes in the top block. In order to prevent the gases from reacting before reaching the substrate, the first 6 cm of the reactor is kept ~200°C cooler than the reaction zone by insulating this region from the heated block. This cool zone ensures that laminar flow is established by the time the gases reach the heated substrate. The bottom block is a 25 cm x 25 cm x 2.5 cm block of nickel and is heated primarily by channel heaters attached to the underside. Two other channel heaters attached to the sides of the block are controlled by an RFL temperature controller. Feedback to the RFL is provided by a thermocouple inserted into the middle of the block. The top block is air-cooled to a temperature ~200°C below the bottom block temperature. The open end of the reactor serves as the exhaust for the the reaction gases and ensures that the reactor is at atmospheric pressure. Substrates are loaded and unloaded through the open end. Details of the apparatus have been previously described.[1]

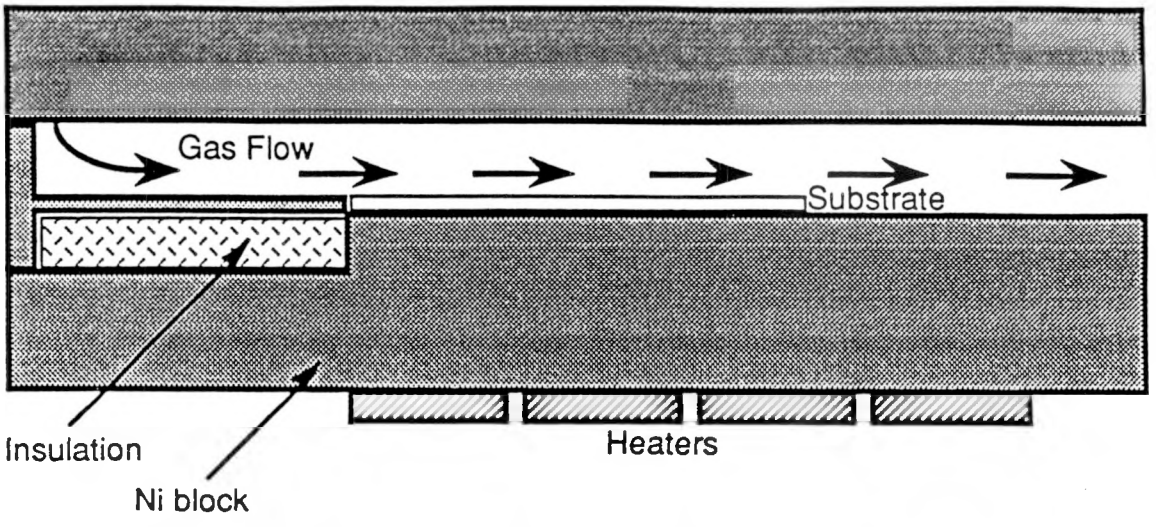

Figure 2. Cross-sectional view of laboratory reactor.

Films were deposited on sodium-free glass substrates (Corning 7059). This glass has a low thermal expansion coefficient which is necessary for maintaining substrate flatness when heated. This glass also has a low visible absorption which is desirable for optical measurements. The concentrations of reagents were 0.1 – 4.5% DMTC, 20 – 80% oxygen, and 0 – 4% Freon. Substrate temperatures were varied from 500°C to 620°C.

4.3 Modeling/Calculations

Spectral transmittance and reflectance data can be used to derive the complex dielectric function, $\varepsilon = \varepsilon_1 - i\varepsilon_2$, or equivalently, the complex refractive index, $N = n - ik$, where n is the refractive index and k is the extinction coefficient. These functions describe the optical properties of the material and are needed both for reliable comparison with theory and for optimizing the performance of a coating. The dielectric function is related to the optical constants by

$$\varepsilon_1 = n^2 - k^2 \ , \tag{1a}$$

$$\varepsilon_2 = 2nk \ . \tag{1b}$$

In principle, ε_1 and ε_2 can be obtained from any two independent spectrophotometric measurements by use of Fresnel's equations. In practice however, experimental uncertainties in the data and the complexity of the equations make analytic computation of ε_1 and ε_2 from measured transmission and reflection values impractical. Instead, the desired information can be obtained by minimizing the difference between the experimental spectrum and a model theoretical spectrum.

Computation of the theoretical spectrum proceeds in two steps. First, the dielectric function for the material is calculated. The most important contributions to the dielectric function in the visible and infrared region are due to interactions of electromagnetic radiation with free carriers, bound electrons, and lattice ions.[2] Since different regions of the electromagnetic spectrum are dominated by different dispersion mechanisms, each of these processes may be treated separately. The reflectance and transmittance are then calculated from the dielectric function. Corrections to the basic thin film model, such as film roughness and thickness inhomogeneities, have been included.

4.3.1 Dielectric Function

The dielectric function can be written as

$$\varepsilon(\omega) = \varepsilon_\infty + \frac{i}{\varepsilon_0\, \omega\, \rho(\omega)} \tag{2}$$

where $\rho(\omega)$ is the dynamic resistivity due to free carriers, $\hbar\omega$ is the photon energy, and ε_0 is the permittivity of free space (= 8.854×10^{-12} A-s/V-m). ε_∞ represents the high frequency limit to the dielectric constant of the undoped tin oxide lattice. The form of the dielectric constant in the infrared region will be described first. A discussion of the corrections necessary in the visible region will follow.

4.3.1.1 Infrared

The simplest approach to modeling the free-carrier contribution to ε is the classical Drude theory.[3] The dynamic resistivity is given by

$$\rho(\omega) = \frac{\gamma}{\varepsilon_0\, \omega_p^{\,2}} + \frac{i\omega}{\varepsilon_0\, \omega_p^{\,2}} \tag{3a}$$

and

$$\omega_p^{\,2} = \left(\frac{n_e\, e^2}{\varepsilon_\infty\, \varepsilon_0\, m^*}\right), \tag{3b}$$

where ω_p is the screened plasma frequency and γ is the scattering frequency, (*i.e.* the probability per unit time that a carrier will undergo a collision). In the Drude model, γ is a constant. The real part of the dynamic resistivity includes scattering effects, whereas the imaginary part is independent of scattering and can be interpreted as the result of the inertia of free electrons.

Despite the fact that real materials are more complicated than the Drude theory suggests, some characteristic properties can be deduced by considering limiting values of the dielectric constant:[4]

1. When $\varepsilon_1 = 0$, the electron gas fulfills the condition for a volume plasma oscillation. At frequencies $\omega < \omega_p$, high reflection occurs. For $\omega > \omega_p$, the reflectance decreases sharply. The plasma frequency is typically regarded as the frequency at which the material changes from dielectric-like behavior to metal-like behavior.
2. If $\varepsilon_1 = 1$ and $\varepsilon_2 << 1$, the index of refraction approaches that of air, which implies that light is transmitted with minimal reflection, at a frequency

$$\omega_{min}^{\,2} = \left(\frac{n_e\, e^2}{(\varepsilon_\infty - 1)\, \varepsilon_0\, m^*}\right). \tag{4}$$

The Drude theory is inadequate as a quantitative model of free-electron properties because γ is introduced as a constant phenomenological parameter whose value can only be fixed by fitting to experimental data. Hence, it gives no clue as to the actual scattering mechanism. Moreover, γ appears to have an energy dependence. Slightly above the plasma energy, there is an abrupt 'knee' in the real part of the dynamic resisivity: at high energies, it follows an $\omega^{-3/2}$ dependence, and at low energies, it is frequency independent.[5] Using experimental values of n_e and γ (determined from the Hall effect and the electrical resistance) to calculate a theoretical reflectivity and then comparing this theoretical spectrum to the experimental spectrum, it is apparent that the Drude

theory does account for the general shape of the of the spectrum; however, some discrepancies are evident. The near IR transmission is higher than predicted by the Drude theory and the wavelength of the minimum reflectivity is off by 5 – 10%.

The Drude theory may be extended by replacing the frequency independent scattering frequency, γ, with a frequency dependent scattering frequency. Formally, γ is replaced by $\gamma_1(\omega) + i\,\gamma_2(\omega)$. Gerlach and Grosse have summarized many sources of electron scattering which may influence the optical properties.[6]

Fluorine atoms in the film not only act as donors giving rise to the electron plasma, they also act as ionized scattering centers for the free electrons. The dynamic resistivity due to ionized-impurity scattering is given by:

$$\rho(\omega) = i\,\frac{Z^2\,N_i}{6\,\pi^2\,\varepsilon_0\,n^2\,\omega}\int_0^\infty k^2\left(\frac{1}{\varepsilon_L(\mathbf{k},\omega)} - \frac{1}{\varepsilon_L(\mathbf{k},0)}\right)dk$$

$$- i\,\frac{\omega}{\varepsilon_0\,\omega_p^2} \qquad (5)$$

where Z is the charge of the positive scatterers, n is the carrier concentration, N_i concentration of scattering centers, and ε_L is the Lindehard dielectric function which includes screening effects. A complete definition of the Lindehard function is described elsewhere.[7]
The real part of equation (5) can be set equal to the real part of equation (3) to find the frequency dependence of the scattering frequency:

$$\gamma(\omega) = \varepsilon_0\,\omega_p^2\,\mathrm{Re}(\rho)\ . \qquad (6)$$

At energies greater than the plasma energy, the scattering frequency follows a $\omega^{-3/2}$ power law. The real part of the resistivity at high frequencies is given by:

$$\rho(\omega) = \frac{Z^2\,N_i\,e^2\,m^{1/2}}{6\,\pi\,(\varepsilon_L(0)\,\varepsilon_0)^2\,n\,h^{1/2}}\,\omega^{-3/2} \qquad (7)$$

The decrease in resistivity with increasing frequency leads to an increase in near infrared and visible transmission over that predicted by the Drude model. Even when ionized impurity scattering is taken into account, discrepancies are still evident. At wavelengths greater than the plasma wavelength, the increase in the reflection coefficient is more gentle than that predicted by the ionized impurity mechanism.

The ionized impurity scattering model assumes a uniform distribution of scattering centers. However, real tin oxide films are polycrystalline, and hence, the distribution of scatterers is inhomogenous. Grain boundaries typically contain higher densities of impurity atoms, lattice mismatch, and voids, all of which contribute to electron scattering. The effect of grain boundaries has been modeled by Proscia.[8] The effective dynamic resistivity is given by an equation derived from an electrical network type analysis of polycrystalline films:

$$\rho_{eff} = \frac{(\,f_1^{\perp}\,\rho_1 + f_2^{\perp}\,\rho_2\,)\,\rho_2}{f_1^{\parallel}\,\rho_1 + f_1^{\parallel}\,\rho_2} \qquad (8)$$

$$f_2^{\perp} = 1 - f_1^{\perp}$$

$$f_2^{\parallel} = 1 - f_1^{\parallel}$$

where, $f_1^{\parallel}$ = volume fraction for **E** parallel to grains,
$f_1^{\wedge}$ = volume fraction for **E** perpendicular grains,
r_1 = complex resistivity of grains,
r_2 = complex resistivity of grain boundaries,
and, **E** = the electric field vector of the incident light.

Ionized impurity scattering is assumed to be the dominant scattering mechanism in the grains, *i.e.* ρ_1 is given by Equation (5). The real part of the resistivity for the grain boundaries is constructed by assuming the scattering in the grain boundaries is some factor, A, larger than the scattering in the grains. The break wavelength, λ_b (wavelength at which grain boundary scattering changes from an asymptotic power law, like equation (7), to frequency independent) and the exponent of the asymptotic power law, p, are allowed to vary in this model. The spectral dependence of these two scattering frequencies is illustrated in Figure 3. The imaginary parts of the resistivity were assumed to be equal. Increasing parameter $f_1^{\parallel}$ decreases the slope of the reflectivity in the region from the plasma wavelength out to the high wavelength limit, and increasing $f_1^{\perp}$ decreases the reflectance at long wavelengths.

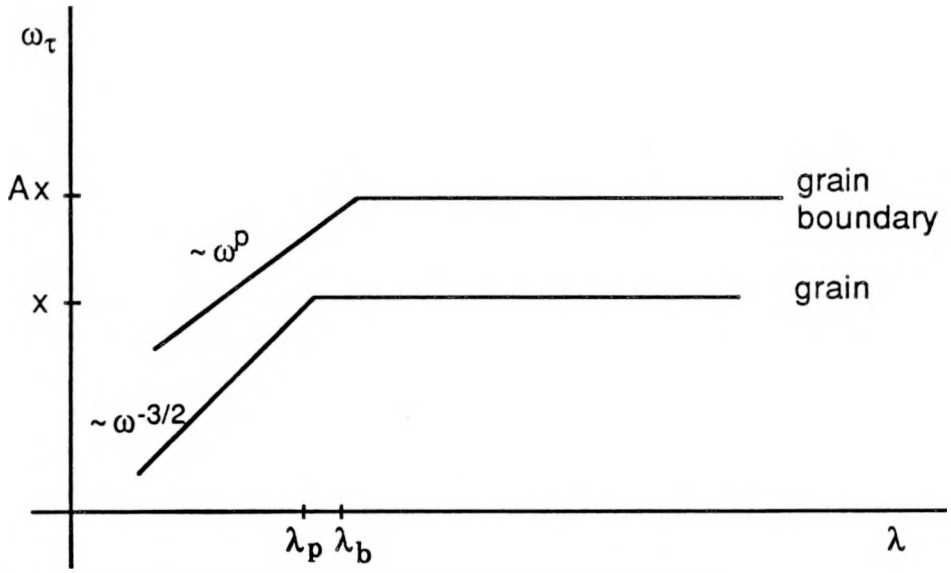

Figure 3. Scattering frequencies in grain boundary model.

4.3.1.2 Visible

The high frequency dielectric constant of tin oxide, ε_∞, is typically taken to be 4.0.[9] However, at higher energies in the blue and uv regions of the spectrum, there is some dispersion in this value. This variation can be modeled by a single, damped Lorentz oscillator, which has a real part described by the following equation:[10]

$$\varepsilon_\infty = p_1 + \frac{p_2\left(1 - \left(\frac{p_3}{\lambda}\right)^2\right)}{\left(1 - \left(\frac{p_3}{\lambda}\right)^2\right)^2 + \left(p_4\left(\frac{p_3}{\lambda}\right)^2\right)} \qquad (9)$$

where p_1, p_2, p_3 and p_4 are parameters determined by optical analysis. The effect of this dispersion may be observed in the reflectance spectrum as an anomalously high interference maximum in the 400-450 nm range. The damped oscillator parameters were determined from a doped tin oxide sample displaying the anomalous high reflectance. In order to minimize effects of band tail absorption, a relatively thin sample was used. The parameter p_4 gives an oscillation in the dielectric constant in the ultraviolet. The best fit was obtained for values: $p_1 = 3.0$, $p_2 = 0.70$, $p_3 = 0.28$, $p_4 = 0.003$.

The effects of absorption due to states in the band gap absorption were treated by adding a standard Urbach-like equation to Equation (2):

$$\varepsilon_{\text{Band Tail}} = i\,\lambda\,U\,e^{a\hbar\omega}\,, \qquad (10)$$

where U and a are parameters determined by the optical fit.[11] Typically, U was about 1.0 μm^{-1} and a was 1.5 x 10^{-2} eV^{-1}.

4.3.2 Reflection and Transmission

Reflectance and transmittance spectra were calculated from the dielectric function using standard optical formulae. These equations, based on Fresnel's equations, take into account the three interfaces (air/film, film/substrate, substrate/air) and multiple reflections in both the film and the substrate.[12] The approach used here accounts for the finite substrate thickness and hence includes the contribution of multiple reflections from the back of the substrate. Previous workers[13] have incorrectly used the semi-infinite approach for thin tin oxide films on glass which could lead to erroneous values of n and k. Corrections for film roughness and thickness inhomogeneity were also included.

The effect of film roughness on reflection and transmission spectra is difficult to treat exactly. In order to accurately characterize the visible absorption, roughness must be taken into account. Surface roughness has two effects: one, it can cause diffuse reflection and transmission (*i.e.* increased non-specular components relative to smooth films), and two, it can act as a gradient in the refractive index. Both effects could affect calculation of absorption. Consequently, roughness has been included in the model. The method of Szczyrbowski[14] was used to calculate the effect of roughness on the transmitted beam. Szczyrbowski treats roughness in terms of an effective gradient in the refractive index. The effect of this correction is to lower the reflection, increase the transmission, and decrease the magnitude of the interference oscillations. Szczyrbowski does not take into account the diminuation of the specularly reflected and transmitted beams that results from the loss of the diffusely scattered components. Consequently, the incident light was attenuated in our model by the factor:

$$1 - S_c = 1 - R_d - T_d \qquad (11)$$

where, $(1 - S_c)$ is the attenuation factor, R_d is the diffuse reflectance and T_d is the diffuse transmittance.

Experimentally, diffuse reflection and transmission spectra were measured and parameterized according to the common scattering power law expressions:

$$T_d = \frac{T_0}{\lambda^m} \quad , \tag{12}$$

$$R_d = f_r \, T_d \quad , \tag{13}$$

where T_0 = parameter related to magnitude of the transmission,
m = parameter describing wavelength dependence,
f_r = fraction of scatter reflected.

For Rayleigh scattering, where the scattering centers are much smaller than wavelength of light, m is equal to four. In Mie scattering, where the scattering centers are much larger than wavelength, m is equal to two. Typical fitted values for m were between 2.4 and 2.8, which are between the theoretical limiting values just mentioned.

The film thickness varies over the beam width of the spectrophotometer. In APCVD, precursor gases become depleted along the flow direction, resulting in significant thickness variations along the flow direction. A thickness gradient can be viewed as the special case of roughness where the wavelength of the incident radiation is much smaller than the average roughness.[15] In this case, the intensity of the interference oscillations decreases, but the average values of reflection and transmission do not change. In the case treated by Szczyrbowski, roughness lowers total reflection and increases transmission in addition to decreasing the magnitude of the oscillations. The thickness gradient was incorporated by calculating the reflection (or transmission) for various thicknesses and averaging[16]

$$R_{avg} = \frac{1}{x_n - x_1} \sum_{i=1}^{n} R(x_i) \, \Delta x \quad . \tag{14}$$

Thickness gradients in the range of 1%-5% of the total thickness were typical.

The spectrophotometer has a finite spectral bandwidth, $\lambda \pm \Delta\lambda$, which is determined by the slit width of the spectrophotometer. The effect of the bandwidth is to shrink the interference fringes. This effect can be minimized by reducing the slit width, but noise problems arise at small bandwidths. The effect is important when width of fringes is of the order of magnitude of $\Delta\lambda$, *i.e.* for thick films.[17] The spectrometer used in this study had a maximum bandwidth of 3.6 nm.

4.3.3 Mobility

As a further test of the grain boundary model, the effective electron mobility was calculated from the routine used to fit the optical data. According to the Drude theory, the bulk conductivity, σ, is simply,

$$\sigma = \frac{n_e \, e^2}{m^* \, \gamma} \quad , \tag{15}$$

and from defining relation for mobility,

$$\sigma = n_e \, e \, \mu \, , \tag{16}$$

solve for μ,

$$\mu = \frac{e}{m^* \gamma} = \frac{63.9 \times 10^{14}}{\gamma} \quad . \tag{17}$$

In this model, the scattering frequency is constant at long wavelengths. Hence, the value of the scattering frequency at the longest wavelength measured (12 μm) was used to calculate the d.c. mobility. Mobilities calculated from the model were typically 1 – 10% larger than the values determined experimentally by Hall measurements combined with resistance measurements. Whereas single crystal mobilities are typically $200 - 250\ cm^2/V\text{-}s$, mobilities for the polycrystalline samples in this study were in the range $10 - 36\ cm^2/V\text{-}s$.[18] Polycrystalline samples generally exhibit lower mobilities than single crystal samples due to carrier scattering in the grain boundaries.

4.4 Experimental Results

Earlier studies have shown that gas-phase chemical reactions play an important role in the CVD process.[19] Concentrations of the reactant species vary along the flow direction due to these homogeneous reactions. Hence, the film growth rate and film thickness are not uniform along the flow. Electrical properties of the films were measured from one sample at four positions in the flow. In Figure 4A, the bulk conductivity is shown as a function of position. The zero position corresponds to the beginning of the hot zone in the reactor. The conductivity does not vary significantly with the position in the flow. Similarly, the other three properties, electron mobility, electron concentration, and fluorine concentration, are nearly constant along the flow direction. These data are shown in Figures 4B, 4C, and 4D.

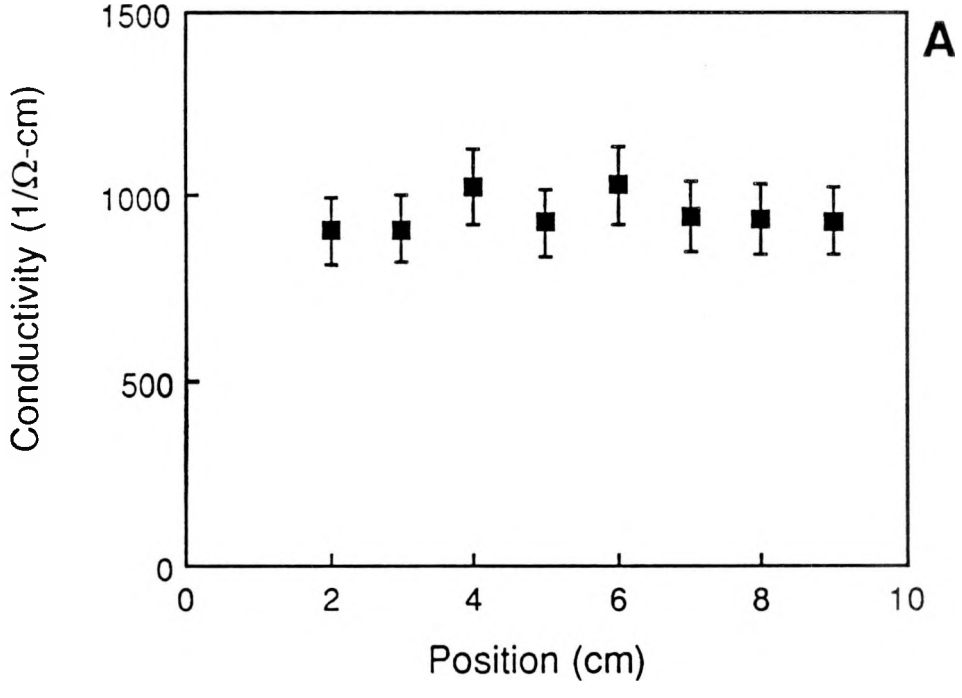

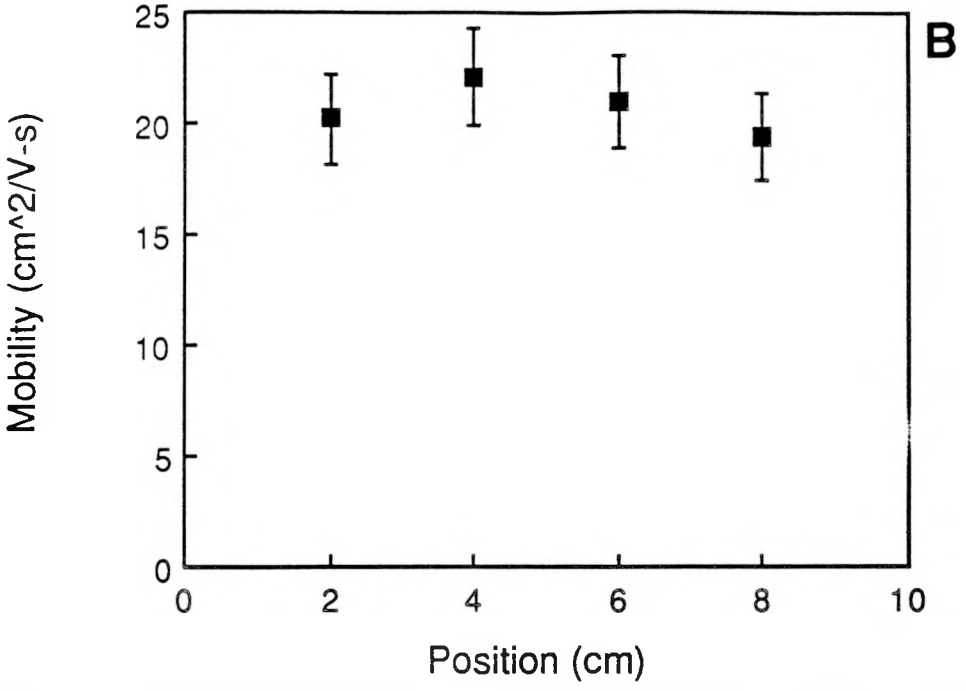

Figure 4. Bulk conductivity (A), electron mobility (B), electron density (C), and fluorine concentration (D) as a function of position in flow.

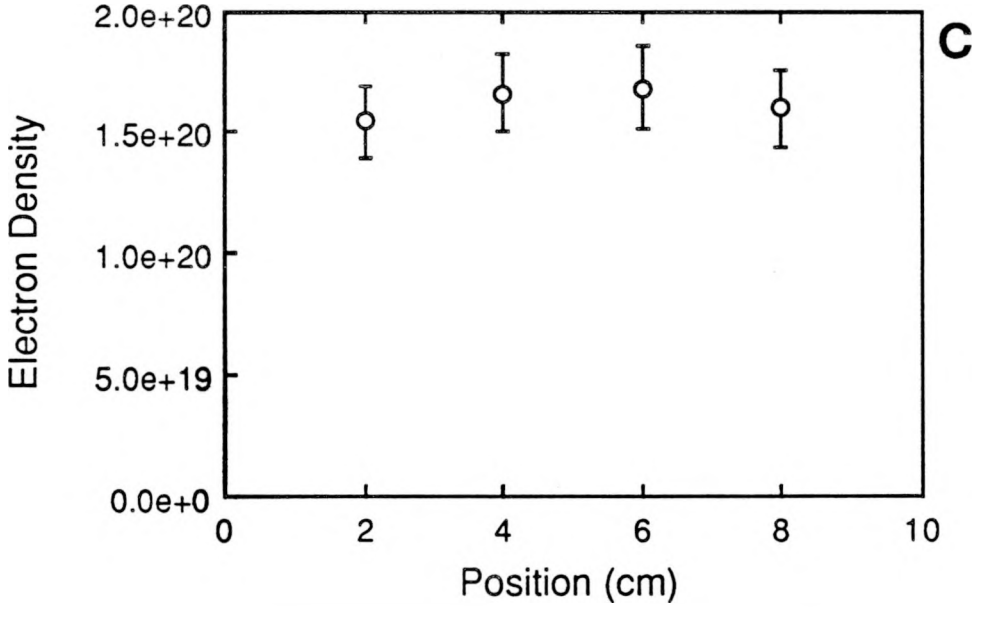

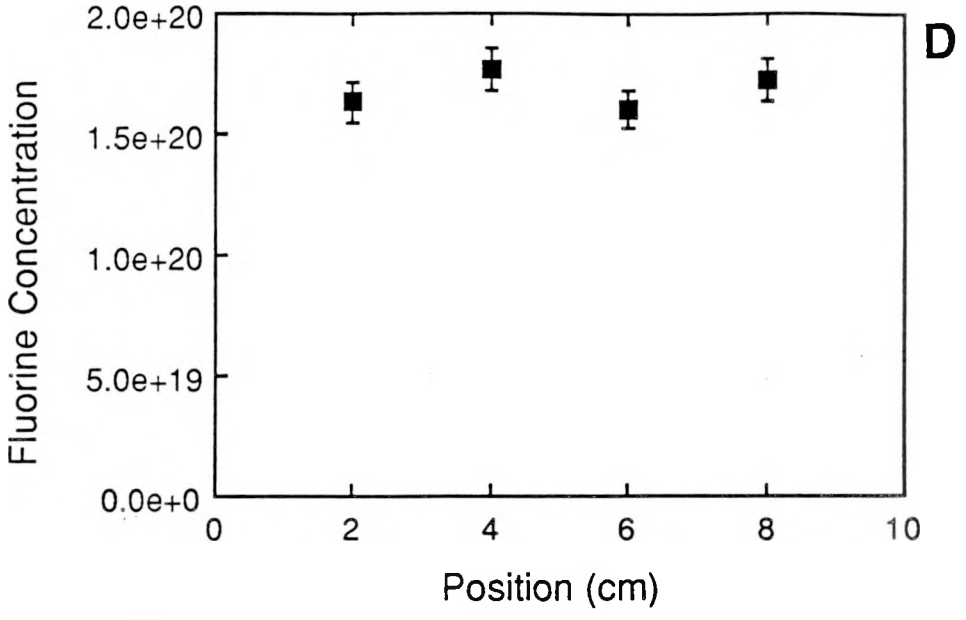

Figure 4 continued.

The bulk conductivity as a function of the deposition temperature is shown in Figure 5. Conductivity generally increases with increasing deposition temperature in the range 500 – 620°C. In Figure 6, the Hall mobility and electron density are shown for the same series of films that were used in Figure 5. The mobility increases by a factor of two in this temperature range. The electron density increases only slightly with deposition temperature. Since the conductivity is proportional to each of these individual properties, the increase in conductivity with increasing deposition temperature can be seen as a result mainly of increasing carrier mobility.

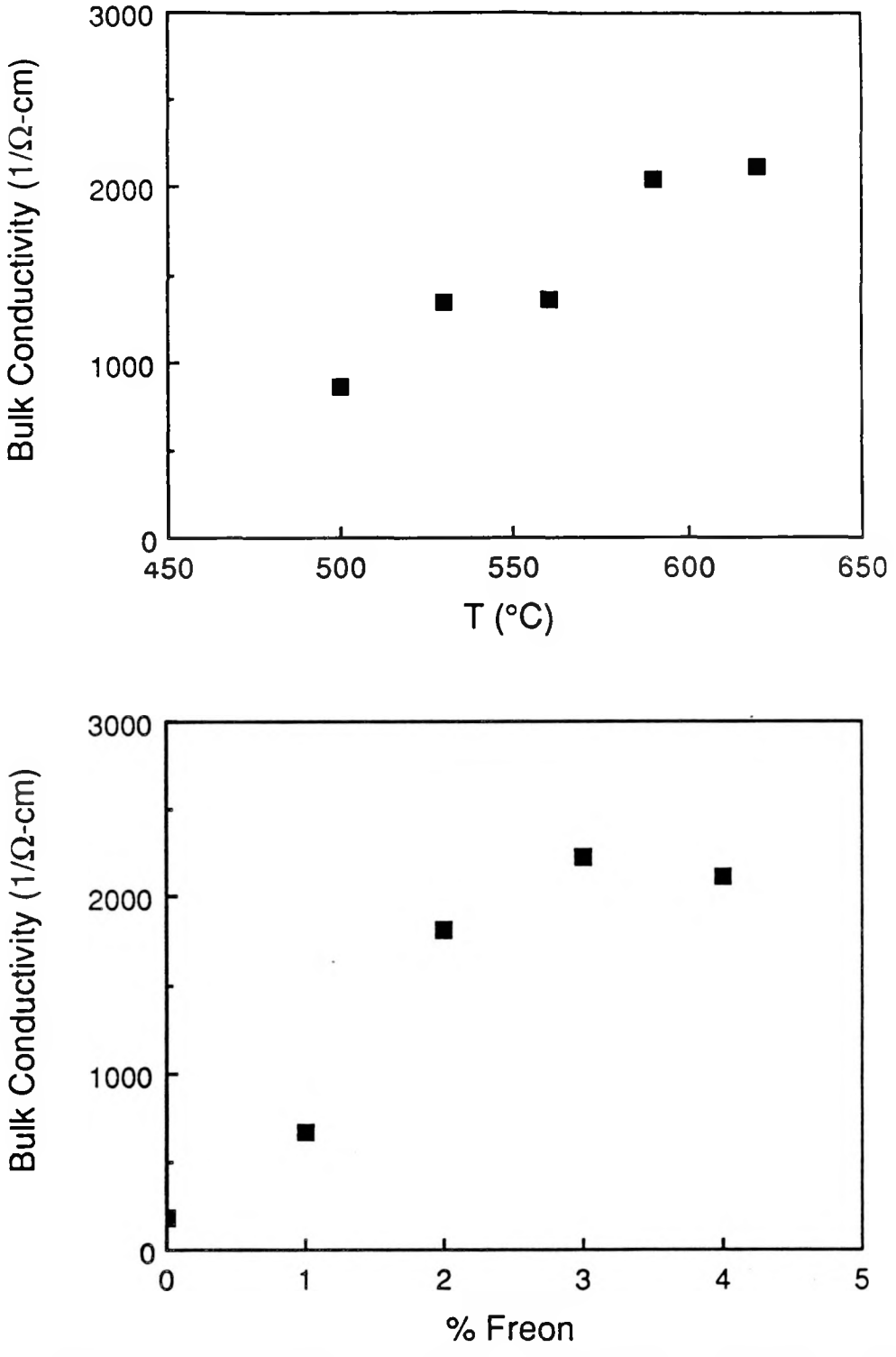

Figure 5. (Top) Bulk conductivity as a function of deposition temperature. (Bottom) Bulk conductivity as a function of Freon concentration.

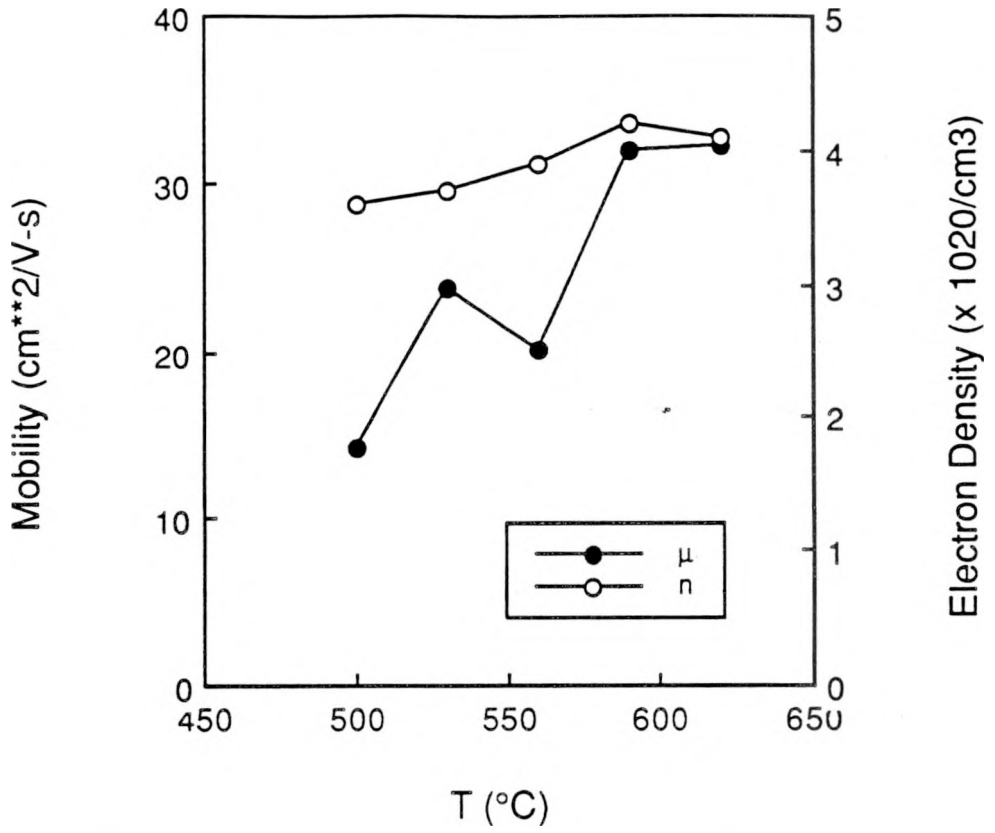

Figure 6. Electron mobility and concentration as a function of deposition temperature.

In Figure 7, the fluorine concentration and the doping efficiency are plotted as a function of deposition temperature. The doping efficiency is simply the fraction of dopant atoms in the film that donate carriers to the conduction band. It can be calculated from the ratio of the electron concentration and the dopant atom concentration:

$$DE = \frac{n_e}{[F]} \quad . \tag{18}$$

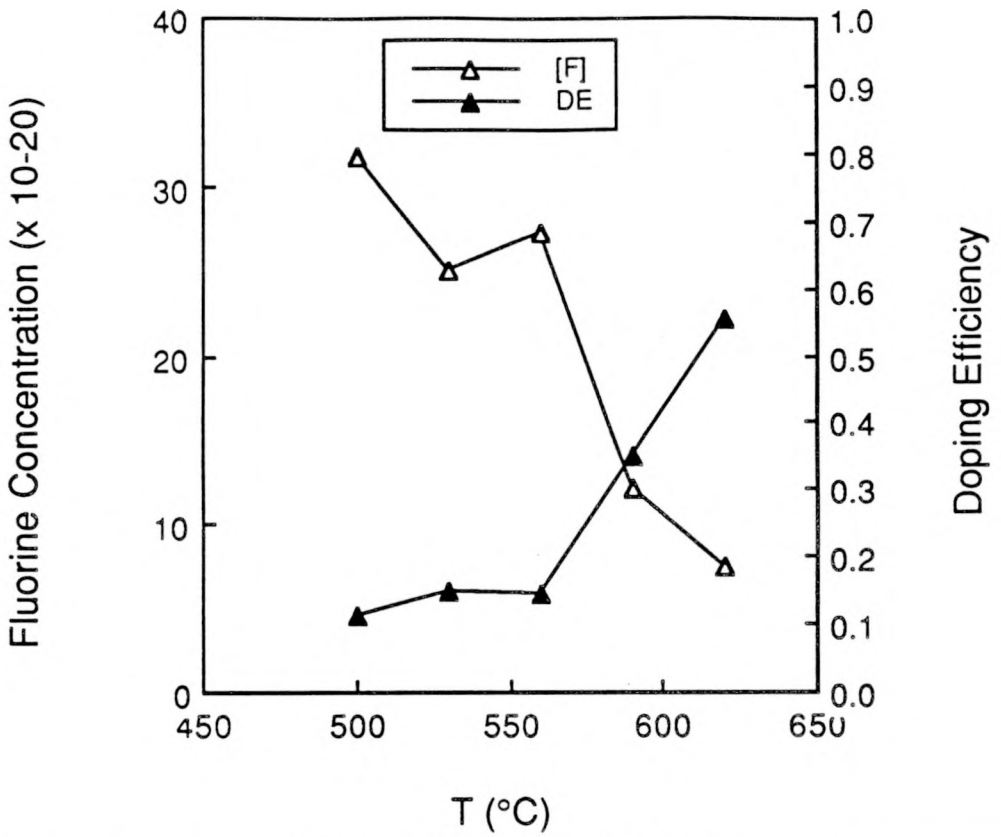

Figure 7. Fluorine content and doping efficiency as a function of depostion temperature.

As deposition temperature increases, the fluorine concentration decreases and the doping efficiency increases. These data show that at higher deposition temperatures, the film contains fewer electrically inactive fluorine atoms. The higher mobility at higher deposition temperatures is consistent with a higher doping efficiency.

The conductivity as a function of Freon concentration is shown in Figure 5B. Increasing the gas phase Freon concentration improves the conductivity. In Figure 8, the Hall mobility and electron density are shown for the Freon series. Both the mobility and electron density increase with increasing Freon concentration. However, the density increases by over a factor of four, while the mobility increases by only a factor of two. In this case, the increase in conductivity with increasing Freon is due more to an increase in the electron density than in the electron mobility. In Figure 9, the fluorine concentration increases by a factor of ten with increasing Freon concentration. The dramatically increasing fluorine concentration coupled with the moderately increasing electron concentration results in a decreasing doping efficiency as Freon concentration increases.

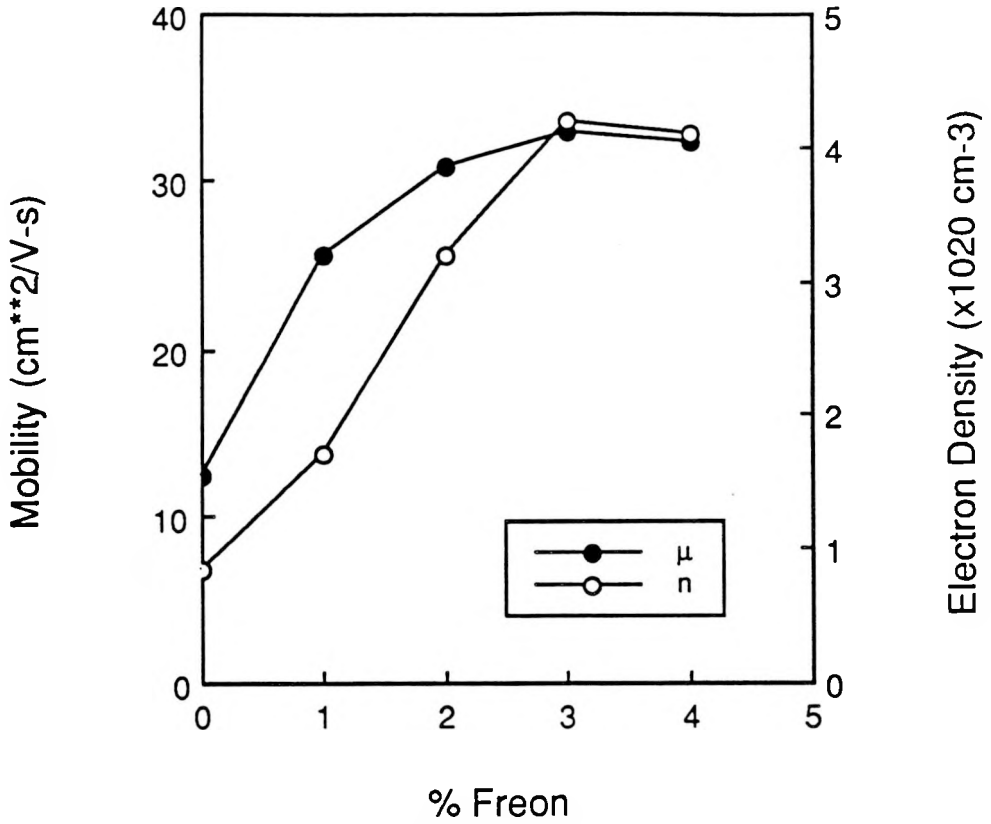

Figure 8. Electron mobility and density as a function of Freon concentration.

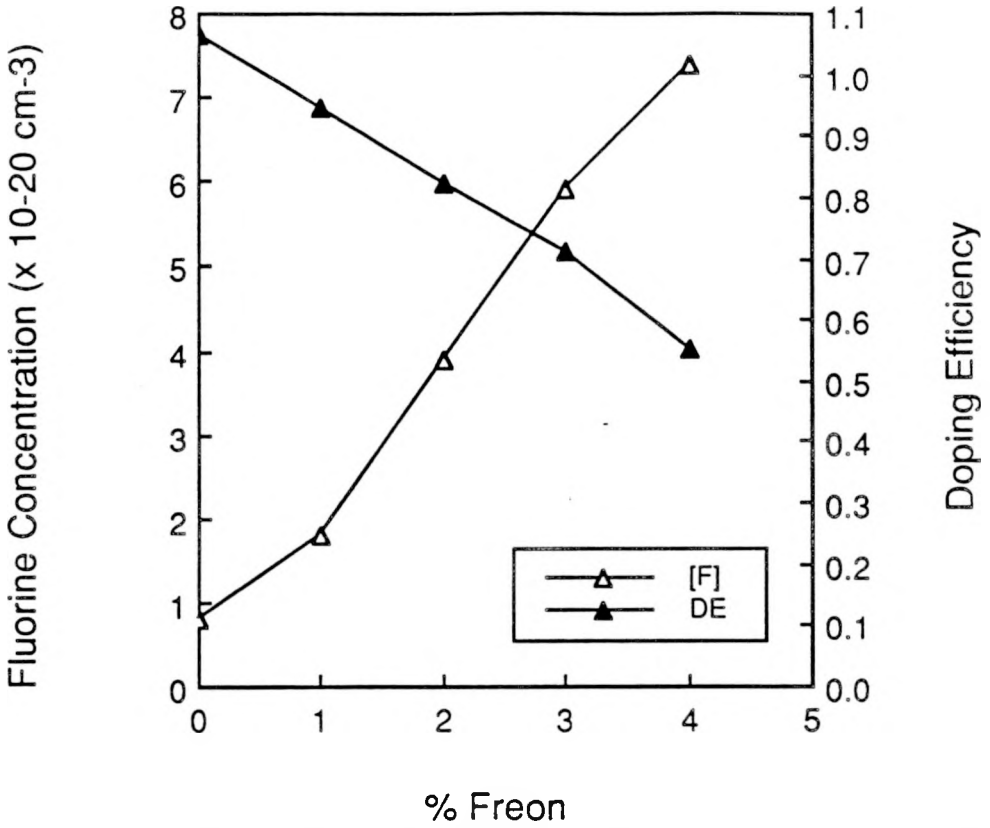

Figure 9. Fluorine content and doping efficiency as a function of Freon concentration.

Diffuse transmission spectra provide a useful way to characterize film roughness. In Figure 10, the diffuse, specular, and total transmission spectra are shown for an 0.8 micron thick sample. The reflection spectra for the same sample are shown in Figure 11. The diffuse and total spectra were directly measured with an integrating sphere, and the specular component was taken by subtracting the diffuse component from the total spectrum. The specular components could also be measured separately in the spectrophotometer without the integrating sphere. The two measurements of the specular component agreed within 1%. For even the roughest films, the diffuse components die out by the infrared region of the spectrum.

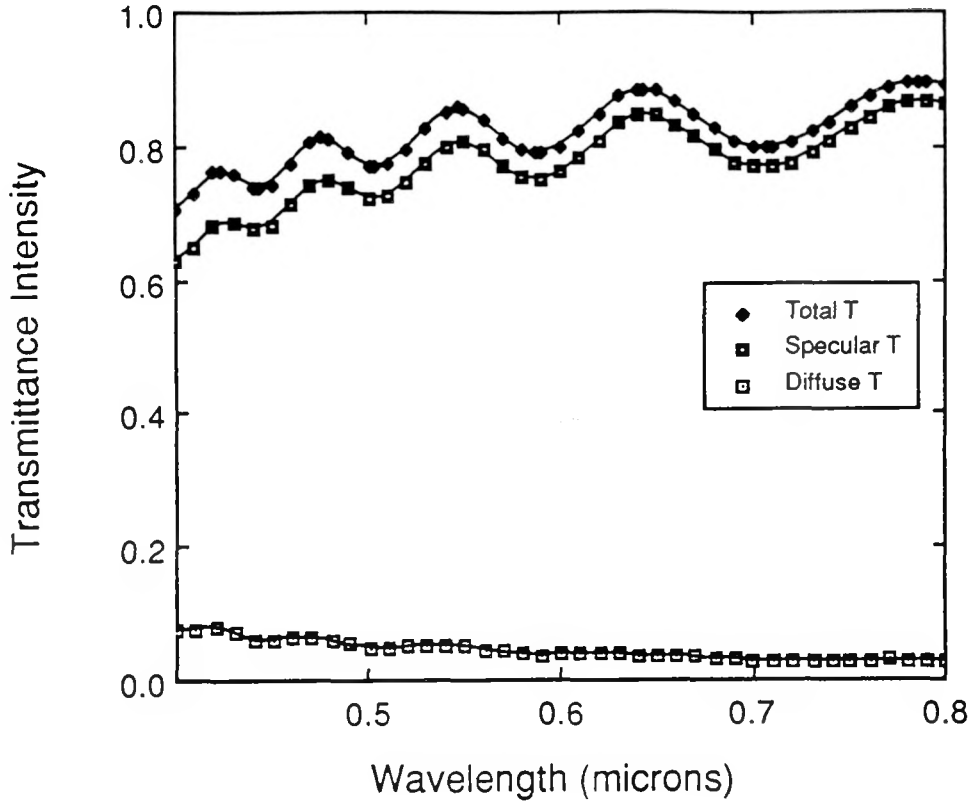

Figure 10. Wavelength dependence of the diffuse and specular components of transmission.

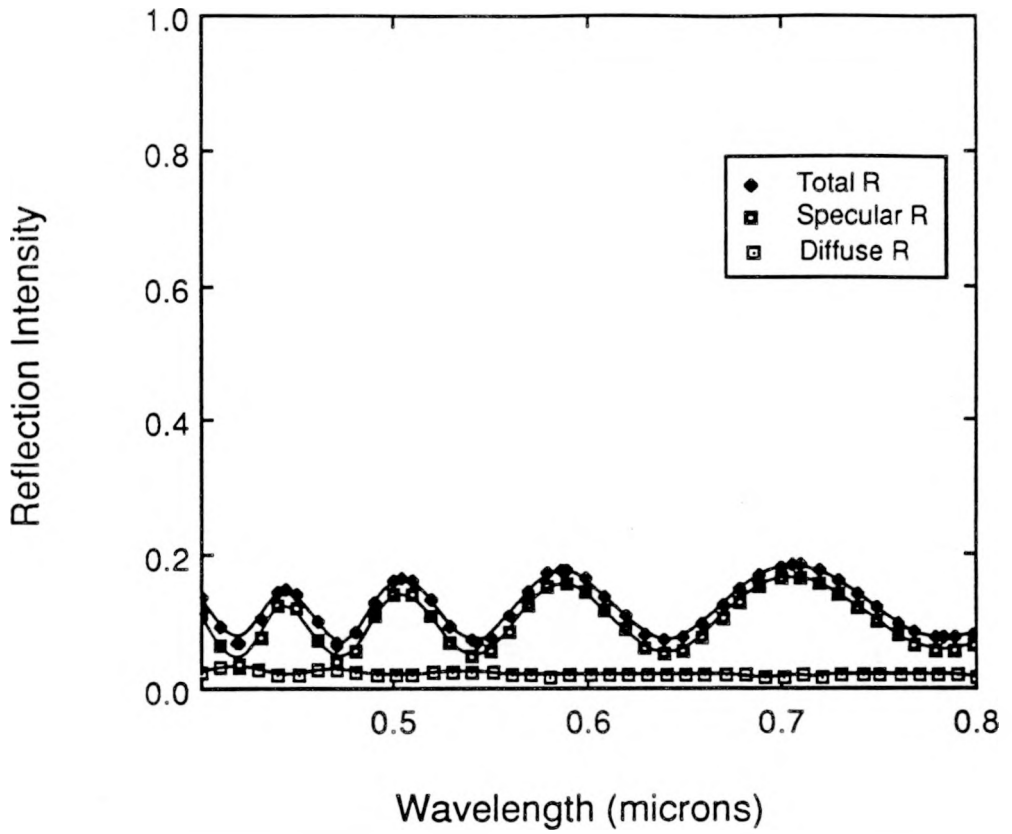

Figure 11. Total, specular, and diffuse reflection spectra for an 0.8 micron thick tin oxide film.

In Figure 12, the diffuse transmission is shown for three films of approximately equal thickness deposited at different temperatures under otherwise identical conditions. As the deposition temperature is increased, the diffuse transmission increases, which suggests that the film roughness is increasing. In Figure 13, the diffuse transmission is shown for three films deposited with differing concentrations of oxygen. (Note that the scale on the y-axis has changed.) Increasing the oxygen concentration from 20% to 80% does not change the growth rate significantly,[20] however, film roughness is dramatically affected.

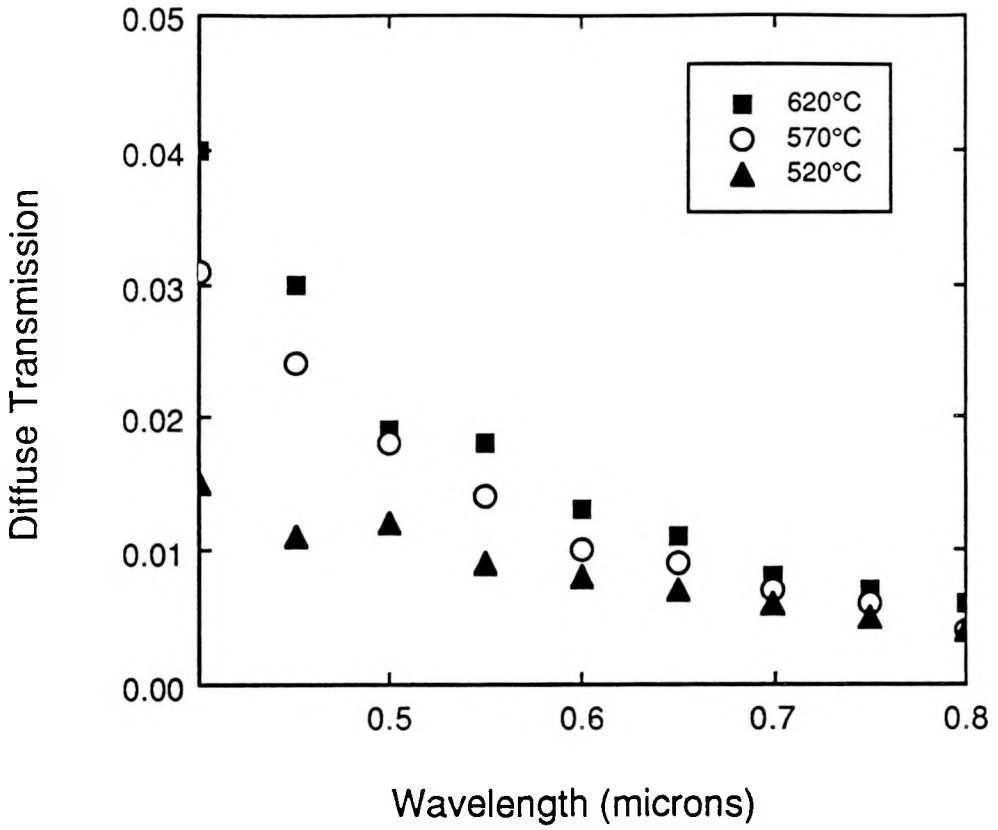

Figure 12. Diffuse transmission as a function of deposition temperature.

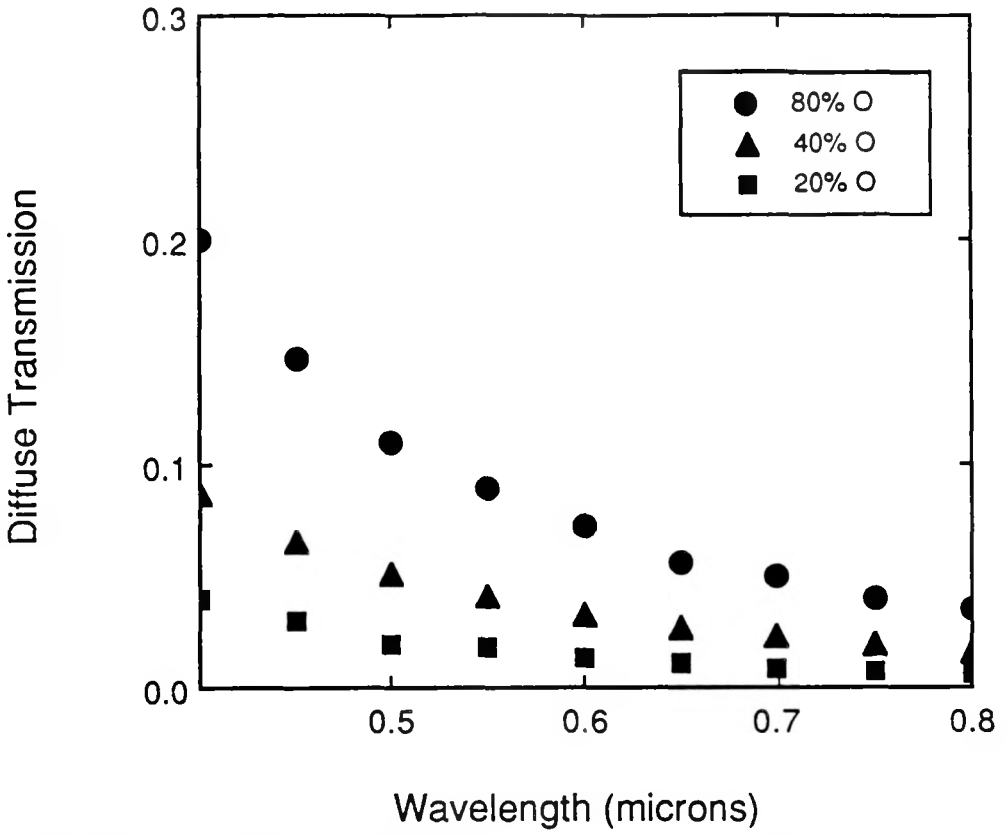

Figure 13. Diffuse transmission as a function of oxygen concentration.

4.5. Modeling Results

Reflection and transmission spectra were fit to the grain-boundary scattering model using a routine (VG02AD) from the Harwell library that minimizes the maximum deviation between experimental and theoretical points. The fitting was done in two steps. First, the infrared reflectance from 2-12 μm was fit by varying six parameters: the free carrier concentration, the volume fractions for parallel and perpendicular grain boundaries, the scattering amplitude in grain boundaries, the break wavelength in the grain boundaries, and the power law exponent in the grain boundaries. The film thickness also needed to be approximately correct in order to fit any points below the plasma wavelength. A value of the effective electron mass for fluorine-doped polycrystalline tin oxide ($m^* = 0.275m_e$) was obtained from the literature.[21]

Fitting the visible data was often more difficult than fitting the infrared data. The visible reflectance and transmittance were fit simultaneously by fixing the six parameters from the infrared fit and varying five other parameters: film thickness, two Urbach tail parameters, thickness gradient, and surface roughness. For some samples, the transmission and reflection spectra were fit separately before attempting to fit both simultaneously. In these cases, the transmission data was used to find the Urbach tail parameters, the film thickness, and the thickness gradient. The reflection data was used to find the surface roughness.

A typical fit of the infrared data is shown in Figure 14. This data is from a sample that was deposited at a substrate temperature of 620°C from 20% oxygen, 2.3% DMTC, 1% Freon. The sample is 0.8 micron thick with an electron density of 1.7×10^{20} cm^{-3}. The agreement between the theoretical spectra and the experimental data is quite good. Table 1 lists the parameters from a series of samples in which the deposition temperature was varied. Table 2 contains the parameters from a series of sample made with varying amounts of Freon. The volume fractions are similar to those observed by Proscia. The perpendicular volume fraction decreases with increasing temperature. The scattering amplitude in the grain boundaries was at least an order of magnitude larger than the scattering amplitude in the grains. The change in the scattering power law occurred at wavelengths (2.2 – 2.9 μm) slightly longer than the plasma wavelength (<2.0 μm). The power law in the grain boundaries was found to vary from -2.2 to -2.7.

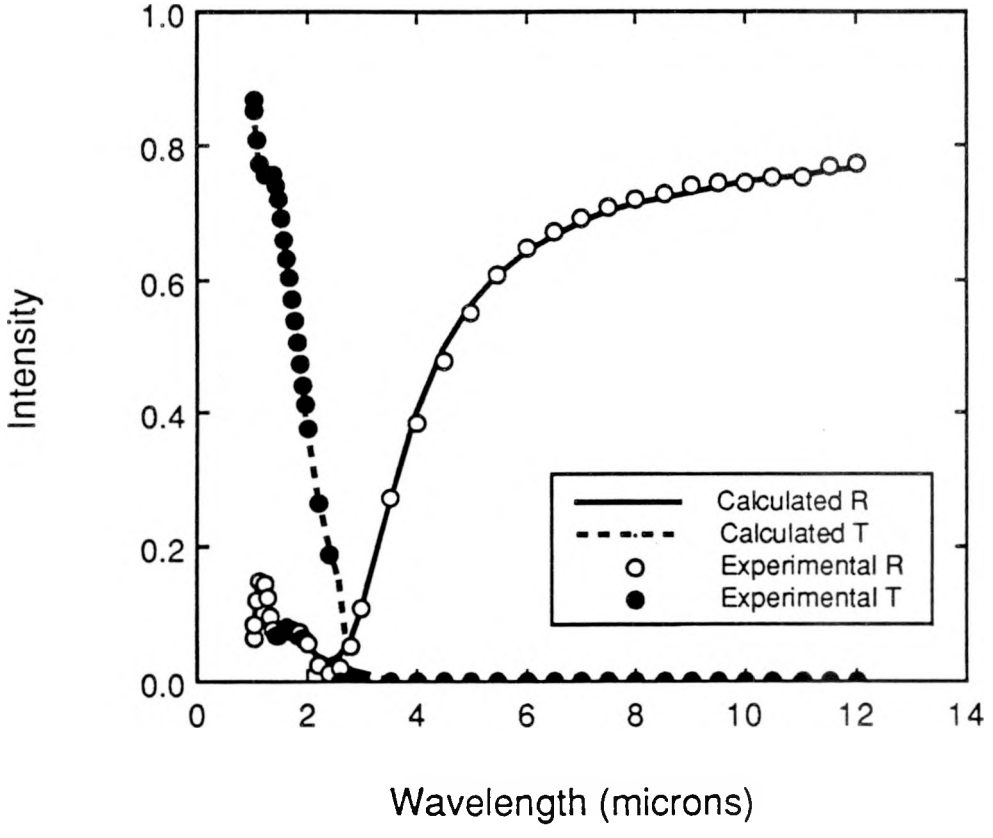

Figure 14. Typical fit of infrared data.

T (°C)	Fr (vol %)	n_e (cm^{-3})	$f_1^{\parallel}$ %	$f_1^{\perp}$ %	A	λ_b (μm)	p
500	4	3.6×10^{20}	17.3	21.0	11	2.3	−2.4
530	4	3.7×10^{20}	19.6	20.2	15	2.2	−2.2
560	4	3.9×10^{20}	18.7	17.2	14	2.4	−2.3
590	4	4.2×10^{20}	21.0	10.8	16	2.3	−2.5
620	4	4.1×10^{20}	19.2	6.1	15	2.9	−2.4

Table 1. Parameters from infrared data for a series of films deposited at varying deposition temperatures.

T (°C)	Fr (vol %)	n_e (cm^{-3})	$f_1^{\parallel}$ %	$f_1^{\perp}$ %	A	λ_b (μm)	p
620	0	0.9×10^{20}	20.8	7.3	14	2.4	−2.3
620	1	1.7×10^{20}	21.5	6.2	13	2.6	−2.7
620	2	3.2×10^{20}	20.8	7.9	12	2.6	−2.2
620	3	4.2×10^{20}	20.6	8.4	13	2.5	−2.4
620	4	4.1×10^{20}	19.2	6.1	15	2.9	−2.4

Table 2. Parameters from infrared data for a series of films deposited at varying Freon concentrations.

A typical fit of the visible data is shown in Figure 15. This spectral data is from the same tin oxide sample as the sample infrared data. From the visible fit, the spectral dependence of the refractive index and extinction coefficient are obtained as shown in Figure 16. The increase in k towards the ultraviolet is due to the Urbach tail, whereas the increase in k towards the infrared is a result of the free-electron properties.

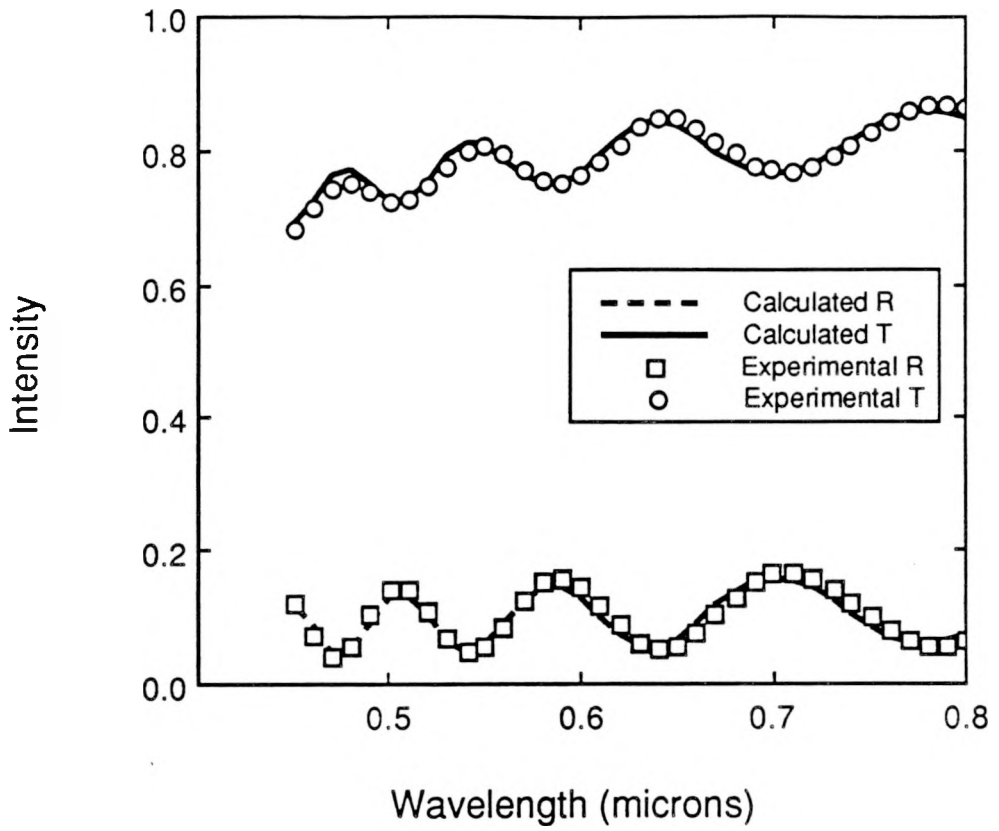

Figure 15. Typical fit of visible data.

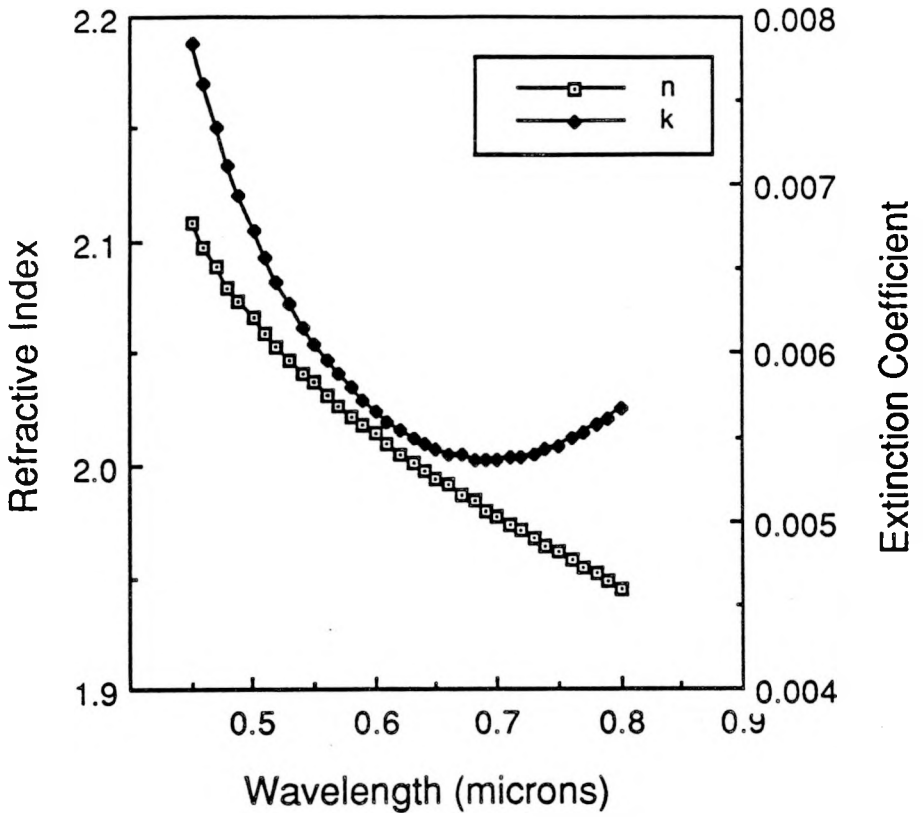

Figure 16. Spectral dependence of refractive index and extinction coefficient.

Table 3 lists the visible parameters for a series of films deposited at varying temperatures. The Urbach tail parameter, U, does not show any correlation with the depostion temperature; however, the parameter, a, does show a general increase with increasing deposition temperature. The film roughness increases with increasing depostion temperature. This increase in film roughness agrees with the increased diffuse transmission that was previously discussed. Table 4 contains the visible parameters for films grown with varying amounts of Freon. The Urbach tail parameters show similar trends with increasing Freon as they did with increasing temperature: U shows no correlation and a increases with Freon concentration. The film roughness decreases with increasing Freon.

T (°C)	Fr (vol %)	Thickness (μm)	U (μm-1)	a (eV-1)	Thickness Gradient	Film Roughness
500	4	0.91	1.0	0.0076	1.2	0.1
530	4	1.1	1.3	0.0098	2.1	0.1
560	4	0.88	0.92	0.0081	1.7	1.2
590	4	0.97	1.1	0.012	3.4	1.5
620	4	0.79	0.94	0.015	1.8	2.0

Table 3. Parameters from visible data for a series of films deposited at increasing temperatures. The concentration of DMTC was 2.3%, the concentration of Freon was 4%, and the concentration of oxygen was 20%. The Thickness Gradient and Film Roughness are expressed as fractions of the film thickness.

T (°C)	Fr (vol %)	Thickness (μm)	U (μm-1)	a (eV-1)	Thickness Gradient	Film Roughness
620	0	0.93	0.95	0.0099	1.0	3.7
620	1	0.88	1.0	0.014	1.6	2.7
620	2	0.95	0.88	0.016	1.4	2.2
620	3	0.76	0.97	0.013	2.2	2.3
620	4	0.79	0.94	0.015	1.8	2.0

Table 4. Parameters from visible data for a series of films with varying Freon concentrations. The concentration of DMTC was 2.3%, the concentration of oxygen was 20%, and the deposition temperature was 620°C.

4.6. Conclusions

The simple resistive-network picture of grain boundary scattering provides a useful theory for modeling the optical properties of these fluorine doped tin oxide samples.

Fluorine doped tin oxide films produced from DMTC exhibit a significant amount of absorption. In order to accurately quantify this absorption, several effects, *e.g.* surface roughness, need to be included in the calculations.

Deposition parameters can be altered to tailor the surface roughness of the film for a particular application. High deposition temperatures, high oxygen concentrations, and low Freon concentrations produce rough tin oxide films. Low temperatures, low oxygen, and high Freon concentrations tend to smooth out the deposited film.

5.0 FLUORINE-DOPED ZINC OXIDE: A NEW TRANSPARENT, ELECTRICALLY CONDUCTIVE MATERIAL

Abstract

A new material, fluorine doped ZnO film, has been produced from vapors of diethyl zinc, ethanol and hexafluoropropene at atmospheric pressure in the temperature range 375°C to 450°C. Information about film composition, orientation and grain size is obtained by electron microprobe, X-ray diffraction and scanning electron microscopy. Electrical and optical measurements for samples deposited at different temperatures and with different fluorine contents show that the film has high conductivity, high visible transmittance and high infrared reflectance for fluorine contents of about 0.5 atomic percent. The thickness, resistance and Hall coefficient measurements were used to determine the film resistivity, electron density and mobility. A simple resistivity network model, which treated the combined effects of ionized impurity scattering and grain boundary scattering , was found to fit the optical and electrical data very well.

5.1 Introduction

Highly conductive and transparent films are widely used in electro-optic devices such as solar cells, liquid crystal and electrochromic displays, optical memories and solar thermal collectors. The most commonly used materials at present for such devices are indium tin oxide (ITO) and tin oxide (SnO_2) [22]. Although ITO films have the desired properties for transparent electrodes, they contain the element indium, which is rather rare and expensive. SnO_2 is less expensive than ITO. However, both ITO and SnO_2 tend to be reduced by hydrogen-containing plasmas, such as those used to deposit hydrogenated amorphous silicon. Also, ITO and SnO_2 tend to absorb in the near-infrared part of the spectrum.

Zinc oxide (ZnO) has attracted interest because it appears to overcome all these limitations of ITO and SnO_2. ZnO resists reduction by hydrogen plasmas better than ITO or SnO_2. ZnO shows high transparency over the whole solar spectrum. Zinc is much less expensive and more abundant than indium or tin. However, pure zinc oxide has a wide band gap of about 3.3 eV [23] and the free electron concentration inside the film is relatively small, which leads to high resistivity and low reflectance in the near infrared and infrared range. If relatively low resistivity can be achieved by preparing nonstoichiometric films or by doping, the less expensive zinc oxide would be an ideal material for transparent and conductive electrodes in solar cells. Nonstoichiometric ZnO films are the simplest and the most economical to prepare, and their electrical and optical properties can be similar to those of indium tin oxide. However, their resistivity at high temperature is relatively unstable. Heat treatment of non-stoichiometric films at 400°C can increase the sheet resistance by factors of 10 to 1000. [24]

On the other hand, doped zinc oxide films can have more stable electrical properties. Many foreign elements such as aluminium, indium [25] and boron [26] have been used to dope zinc oxide to high electrical conductivity. However, a disadvantage of the group III dopants is that they greatly reduce the mobility of the free electrons in doped zinc oxide. A qualitative argument for this effect is as follows. Group III atoms presumably become electrically active as n-type dopants in zinc oxide when they substitute for zinc atoms. In a relatively ionic semiconductor like zinc oxide, the conduction band derives mainly from the metal (zinc) orbitals. Thus every dopant metal atom represents a strong local perturbation to the conduction band, which causes strong scattering of the electrons in the conduction band, thereby reducing their mobility. On the other hand, dopants

which substitute for oxygen, rather than zinc, would perturb mainly the valence band, leaving the conduction band relatively free of scattering, with a higher electron mobility. Halogen atoms substituting for oxygen would therefore be expected to be n-type dopants which retain high electron mobility. The heavier halogens, chlorine, bromine and iodine, are too large to substitute for oxygen without large distortions of the crystal lattice. However, fluorine ions are about the same size as oxide ions, and thus fluorine would be predicted to be an n-type dopant which maintains high electron mobility in zinc oxide. A second disadvantage of these group III elements is that they can also dope amorphous silicon films. Out-diffusion of these dopants from the doped zinc oxide into the amorphous silicon can degrade the cell efficiency either during deposition or in use, and so it is desirable to find a dopant for zinc oxide which is not electrically active in amorphous silicon. Fluorine, which is known to be electrically inactive, or even beneficial, in hydrogenated amorphous silicon, satisfies these conditions and would therefore be an ideal dopant.

Deposition of zinc oxide has been achieved by chemical vapor deposition (CVD) [27] [28], rf magnetron sputtering [29], reactive sputtering [30], vacuum evaporation [31] and spray pyrolysis [32]. Chemical vapor deposition is especially useful for large scale coating at a high growth rate. Many chemicals containing oxygen atoms such as oxygen, water, nitrous oxide, alcohol and even carbon dioxide have been successfully used to react with organometallic zinc compounds to produce zinc oxide films. The most commonly used zinc compounds are diethyl zinc (DEZ) [33] and dimethyl zinc (DMZ) [34]. Although the latter can react with oxygen at atmospheric pressure to coat the substrate over a large area at a reasonable growth rate [35], it is more expensive and dangerous. Diethyl zinc is much cheaper and has been widely used to deposit both pure and doped zinc oxide films. It is difficult to control the reaction of DEZ with either oxygen or water because premature reactions upstream from the substrate can produce powder at high concentrations of the reactants. The reaction between DEZ and alcohol depends on the alcohol used and the deposition temperature [28], and so uniform films can be produced at reasonably high growth rates by choosing different alcohols at different temperatures.

In this paper we will demonstrate for the first time that fluorine is a highly active n-type dopant in zinc oxide films. The fluorine doped zinc oxide films have been successfully deposited from diethyl zinc, ethyl alcohol and hexafluoropropene. Resistivity measurements, ellipsometry, X-ray diffraction, SEM and Hall coefficient measurements are used to characterize the properties of the film. Electron microprobe analysis is used to determine the film composition. A simple theoretical model is used to treat the combined effects of grain boundary and ionized impurity scattering on the infrared and visible reflectance and transmission data. The fluorine-doped zinc oxide films show higher electron mobilities than other doped ZnO films. Their properties are stable to temperatures of at least 450°C.

5.2 Experiment

The ZnO deposition apparatus is shown schematically in figure 17. The nickel reactor has a special nozzle, designed by the Watkins-Johnson Company, with three separated gas-inlet lines. This design is helpful in moderating the fast reaction of DEZ and ethanol at high temperatures. The inner line and the outer lines are used to introduce DEZ and ethanol vapor, respectively. The middle line is for buffer helium which keeps DEZ and ethanol separated for a small distance after being injected into the reactor. The reactor is a rectangular chamber 1cm high, 12.5cm wide and 30cm long. Substrates rest on the bottom of this chamber. The reactor was put on a hotplate, and the thermocouples for the temperature controller were inserted in holes in the bottom plate of the reactor. The deposition temperature can be stabilized to ±1°C, and the deposition reaction of DEZ and ethanol was studied over the temperature range from 300°C to 450°C at atmospheric pressure. An oven was used to heat the alcohol bubbler to 60°C in order to achieve a high vapor pressure and the temperature of the DEZ bubbler was kept at 25°C throughout the experiments. The DEZ and alcohol vapors carried away by helium from their bubblers were further diluted by the pure

helium from dilution lines. The gas flow for DEZ, ethanol and buffer lines were each 4.0 l/min and therefore the total gas flow was fixed at 12.0 l/min. The DEZ and alcohol concentrations in the gas mixture were calculated by assuming that the carrier helium was saturated in each bubbler. An extra port attached to the alcohol dilution line was used to introduce the dopant gas. A four-port valve and a three-port valve controlled by an air-actuator and a timer were used to switch on and off the reactant gases.

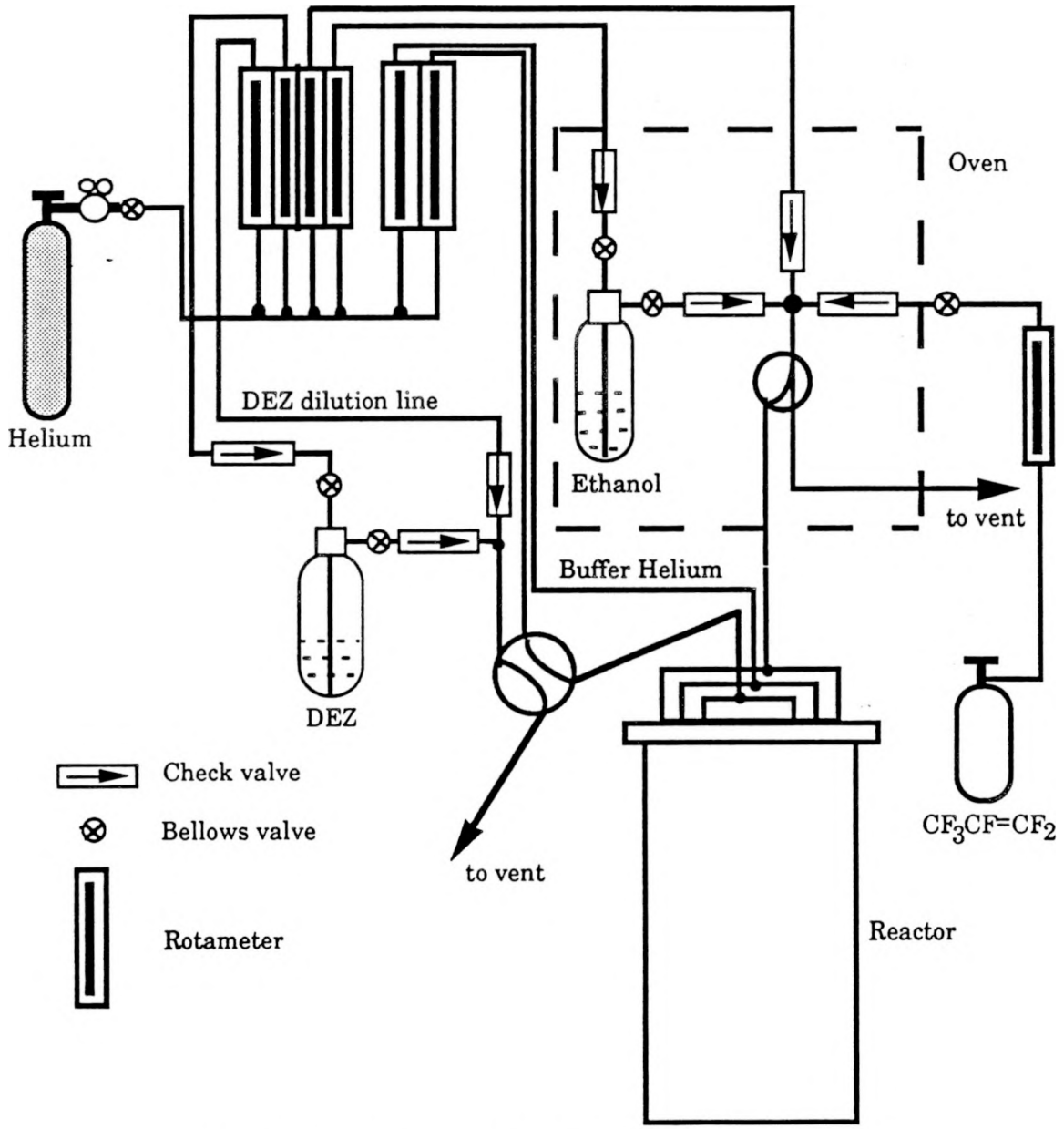

Fig.17 Schematic diagram of the ZnO film deposition system.

The thicknesses of films below 1500Å were measured by using a Rudolph Research AutoEL-II ellipsometer to determine their thickness and refractive index. The best results are obtained for a thickness above 500Å and below the full cycle thickness (usually about 1900Å for ZnO films with a refractive index of about 1.95). Thicknesses of thicker films were determined by fitting visible

reflectance data. For fixed DEZ concentration and deposition temperature of 350°C, we found the alcohol concentration giving the highest growth rate. When the dopant experiments were carried out at higher temperatures, these optimized alcohol and DEZ concentrations were employed.

After the doped films are deposited, the sheet resistances were measured, and mid-infrared reflectance spectra and near infrared and visible reflectance and transmission spectra were taken. X-ray diffraction measurements and scanning electron microscopy(SEM) gave useful information about crystallite orientation and size. Hall effect measurements combined with the measured resistivity determined the free electron concentrations and Hall mobilities. Electron microprobe analyses determined the film composition. The results from a theoretical optical model were compared with the infrared and visible spectra.

5.3 Results and Discussion

5.3.1 Film Deposition

The thickness of a film can be used to determine the growth rates of the CVD reaction between DEZ and ethanol. The film growth rates are obtained from samples deposited with thickness below 1500Å by controlling the deposition time. Figure 18 is a plot of undoped film thickness as a function of the position from the gas inlet. The reactant concentrations have been chosen to maximize the peak growth rate at a deposition temperature of 400°C. Figure 18 also showed the film refractive index at a wavelength of 632nm determined from ellipsometry. The refractive index was found to depend on the film thickness and differ slightly from that of the bulk ZnO crystal which is 2.03 [33]. This thickness dependence of refractive index may result from the density dependence on the film thickness. Usually a thicker film has higher density than that of a thinner film because the film is deposited layer by layer on the substrate and a density gradient exists in the direction perpendicular to the substrate. As the film becomes thicker, its density should approach that of the bulk ZnO.

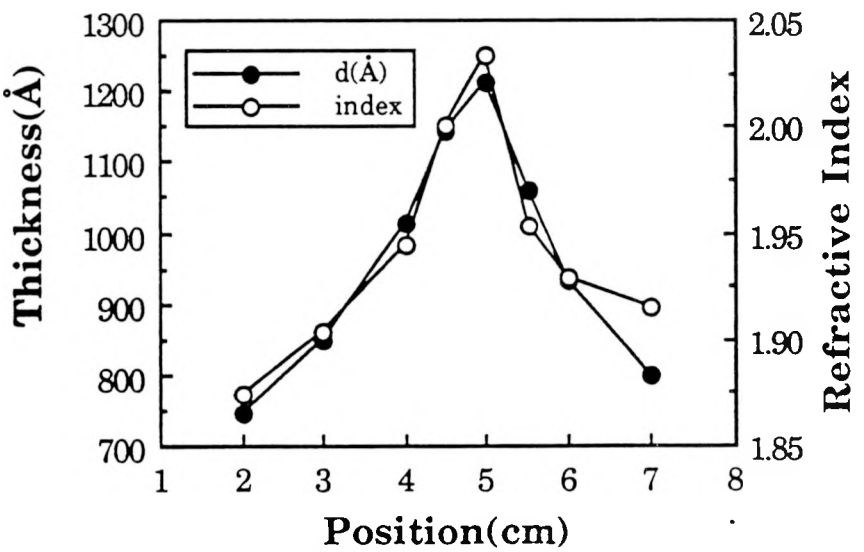

Fig. 18. Film thickness and refractive index at λ = 6320Å as a function of the position on the substrate. The DEZ and ethanol concentrations are 2.60×10^{-5} mol·l^{-1} and 1.54×10^{-3} mol·l^{-1} and the deposition temperature is 400°C.

Figure 19 shows that at 350°C and a total gas flow of 12.0 liters/min, the peak growth rate of ZnO for a fixed DEZ concentration first increases with increasing ethanol concentration in the gas mixture. However, higher ethanol concentrations decrease the growth rate. When the DEZ concentration in the reactant gas is 2.60×10^{-5} mole/l at 25°C, the highest growth rate is found for an ethanol to DEZ mole ratio about 60.

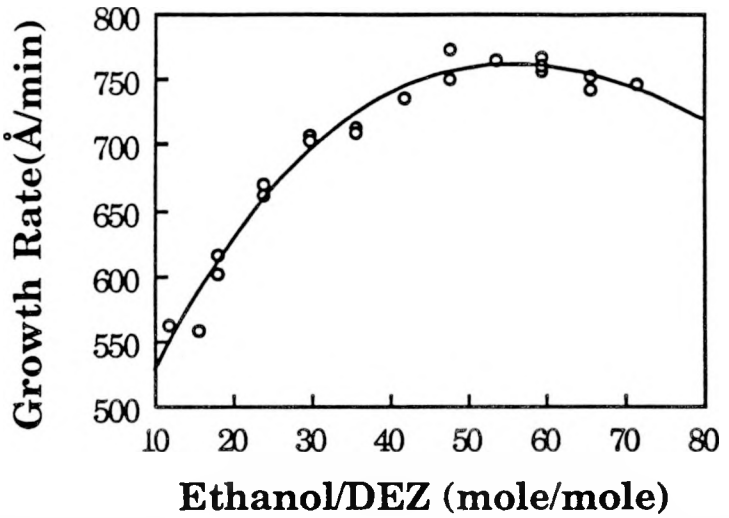

Fig. 19. Growth rate as a function of the concentration ratio of ethanol to DEZ. The deposition temperature is 350°C and the DEZ concentration is 2.60×10^{-5} mol·l^{-1}.

Figure 20 is a plot of peak growth rate vs DEZ concentration for fixed ethanol concentration of 2.42×10^{-3} mole/l. In the low DEZ concentration region, the growth rate depends linearly on DEZ concentration. As more DEZ is introduced into the reactor, white "smoke" can be seen coming out of the reactor and the measured peak growth rate increases more slowly. In order to have a linear increase in the film growth rate, an ethanol to DEZ mole ratio greater than 60 is needed to insure the complete oxidation of diethyl zinc.

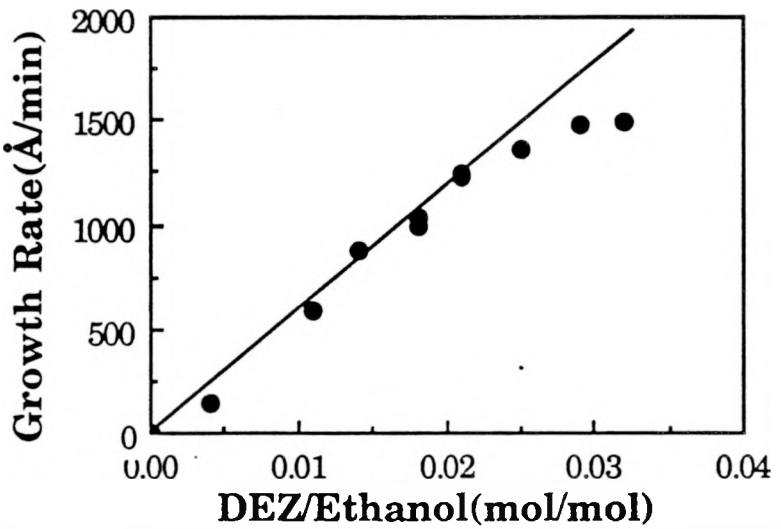

Fig. 20. Growth rate as a function of the concentration ratio of DEZ to ethanol. The deposition temperature is 350°C and the ethanol concentration is 2.42×10^{-3} mol·l^{-1}

From figure 21 we see that the growth rate increases with temperature much faster in the high temperature range than in the low temperature range. This temperature dependence of the growth rate observed in our experiments is different from that reported in the literature [28]. This difference may lie in the reactor geometry. It is also found that film can cover larger areas and become a little more brownish and more translucent as the deposition temperature increases. The translucency may result from the roughness of the film which produces more light scattering centers on the surface. Above 375°C the roughness of the film increases very fast and the ellipsometer becomes less reliable for the determination of film thickness; thus no thickness measurements were done for temperatures above 425°C.

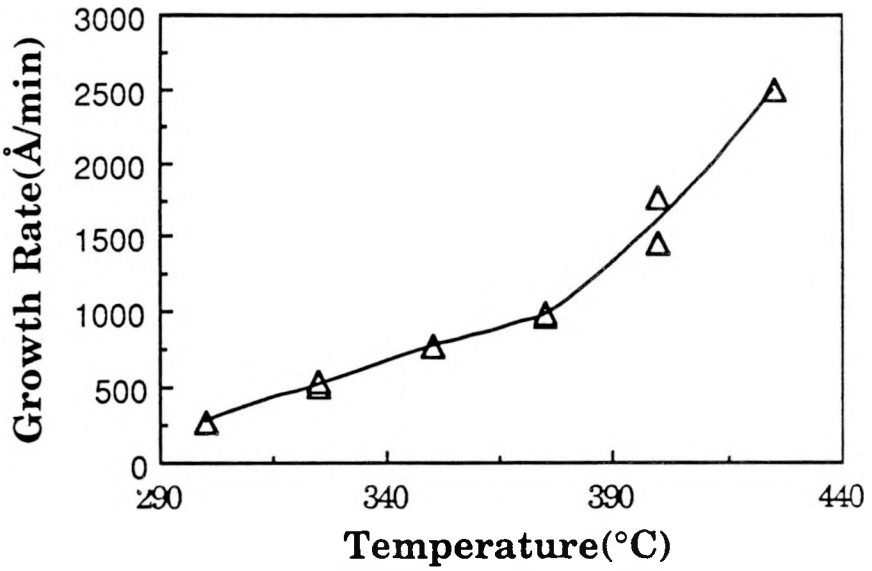

Fig. 21. Growth rate of ZnO film as a function of substrate temperature. The concentrations of DEZ and ethanol are 2.60×10^{-5} mol·l^{-1} and 1.54×10^{-3} mol·l^{-1}, respectively.

The dopant gas hexafluoropropene has some influence on the film growth rate and roughness. As the dopant gas flow increases, the film growth rate also increases slightly and a smoother film can be obtained even at higher temperatures.

5.3.2 Electron Microprobe and Film Composition

A Cameca MBX electron microprobe equipped with a Tractor Northern TN-5502 EDS system and a TN-1310 wavelength dispersive spectrometer is used to determine the film composition. The used standard for Zn and fluorine are pure ZnO and CaF_2. The oxygen concentration is difficult to determine directly because of the oxygen-containing substrate. Instead, oxygen atomic percentage was found by the difference from 100% after the atomic percentages of other elements were known. The results usually gave a very small amount of excess zinc compared with oxygen, which shows that the film is non-stoichiometric. This excess zinc in the film is the reason that the non-doped films still have measurable resistance. The fluorine content was found to vary from 0.1 to 1.0 at.% for highly conductive ZnO films. The fluorine concentration in the film is shown in figure 22 as a function of the distance from the gas inlet. The inhomogeneous composition along the gas flow is a typical feature of CVD processes in which gas phase reactions alter the composition of the gas phase along the flow direction. Usually the position of highest growth rate is not the same as the position of highest fluorine content. Higher dopant gas flow and lower deposition temperature (at least above 375°C) can usually increase the fluorine content to some

extent. Table 5 shows the compositions of films deposited at different temperatures. The samples were selected from the most conductive parts on the substrate. At constant dopant gas flow, more fluorine usually can be incorporated into the film as the temperature increases. However, higher temperatures lead to a more rapid increase in the film deposition rate than in the fluorine incorporation rate, and thus a lower fluorine concentration in the film. The electron microprobe is not a good method to determine carbon content and no attempt was made to detect carbon. Other methods such as XPS detected carbon on the film surface but only a very small amount of carbon could be detected after the surface layers were sputtered away.

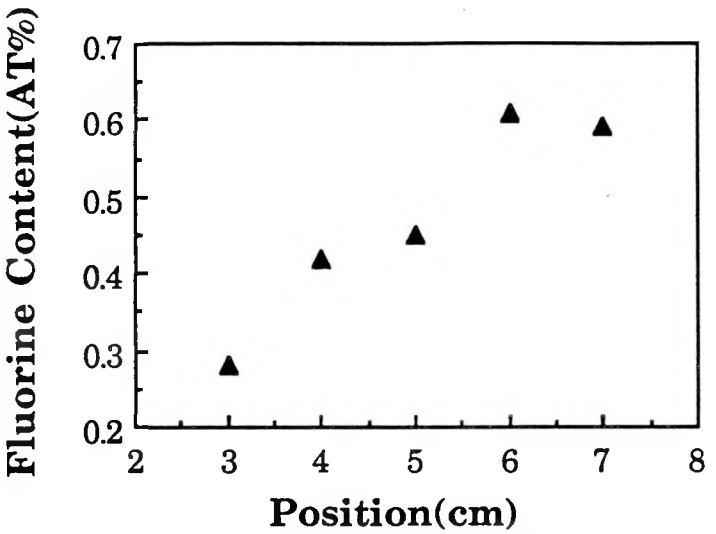

Fig. 22. Fluorine content as a function of the distance from the gas inlet. The deposition temperature is 400°C. The DEZ and ethanol concentrations are 2.60×10^{-5} mol·l^{-1} and 1.54×10^{-3} mol·l^{-1}, and the hexafluoropropene concentration is 5.79×10^{-5} mol·l^{-1}.

Table 5. Compositions of ZnO films and their deposition temperatures. The DEZ and ethanol concentrations determined at 25°C are 2.60×10^{-5} mol/l and 1.54×10^{-3} mol/l and the dopant gas hexafluropropene is 5.79×10^{-5} mol/l.

Sample	Temperature ℃	Zinc at.%	Oxygen at.%	Fluorine
A	375	52.2	47.2	0.62
B	390	51.6	47.8	0.58
C	400	50.1	49.4	0.48
D	410	49.9	49.7	0.42
E	450	48.4	51.3	0.25

X-ray diffraction and SEM

X-ray diffraction measurements were made on a Philips powder crystallography instrument by using copper K_α radiation (λ = 1.54 Å) for films deposited on soda lime glass at temperatures ranging from 325°C to 425°C. Figure 23 shows an X-ray diffraction spectrum of ZnO film deposited at 400°C. Only the (002) diffraction peak can be observed and the film therefore has a high-c axis orientation perpendicular to the plane of the film. At both higher and lower temperatures, the films are less oriented and other diffraction peaks can be observed. Although the

(112) peak appears on the spectra of films deposited at 325°C and the (101) peak is not visible, the opposite situation is observed for films deposited at 425°C for which the (112) peak disappears and (101) can be observed. However, it is very difficult to determine the effect of the crystallite orientation on film properties because of the concurrent increasing crystallite size. The dopant was found to have no influence on the diffraction peak of the film and the doped film at 400°C still has a high c-axis orientation.

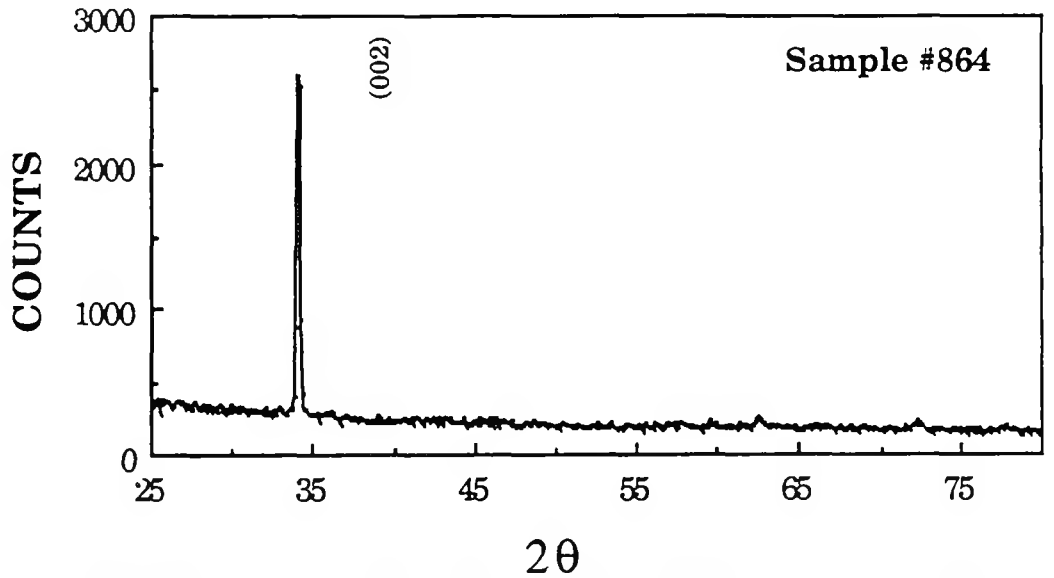

Fig. 23. X-ray diffraction spectrum of ZnO film deposited at 400°C on soda lime glass.

The powder diffraction line width can be used to estimate the grain size of the film. If the crystals in the films are smaller than 1.0 μm, the diffraction peak will be broadened, while for crystal sizes greater than about 1 μm, the width of the diffraction line will be determined by the instrument. Let B_s be the measured peak width of a standard sample with large crystal size (greater than 1μm) and B_m that of the sample to be measured. Then by assuming the diffraction peak to be an error curve, we can find the broadening of the peak B from $B^2 = B_m^2 - B_s^2$ and the grain size can be estimated from the Scherrer formula [36]. Figure 24 shows that larger grain sizes can be obtained from higher deposition temperatures.

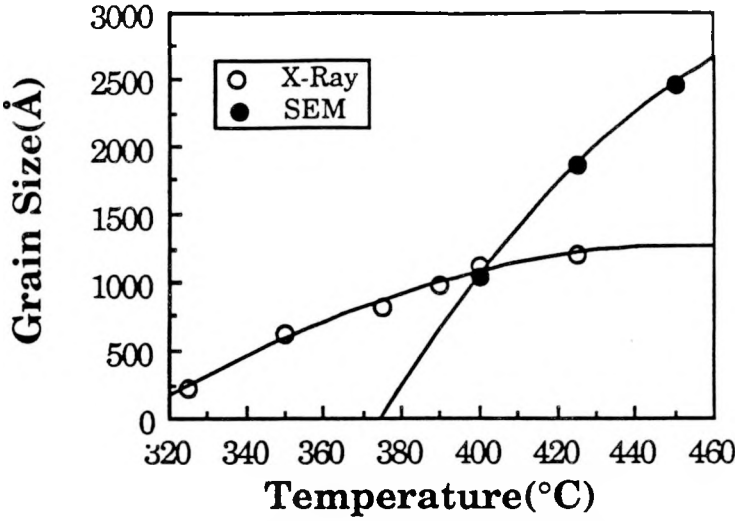

Fig. 24. Grain size of polycrystal ZnO film as a function of deposition temperature.

Scanning electron micrographs were taken on a JEOL JSM-35 scanning electron microscope. Figure 25 shows a few electron micrographs for films deposited at different temperatures. The film deposited below 350°C shows no structure and the grain size could not be determined from its micrograph. As the deposition temperature was increased to 400°C, the crystals could be seen to be globular and they almost completely cover the whole substrate. At still higher temperatures the crystallites become larger and hexagonal and there are "holes" between crystallites and the film can be expected to be less dense than the bulk zinc oxide. The hexagonal crystallites clearly indicate that the film is oriented with c-axis perpendicular to the substrate, which is consistent with the information revealed by X-ray diffraction. The grain sizes determined from micrographs are different from those obtained by X-ray diffraction. This difference can be explained by the fact that micrograph is an image of the horizontal size of the crystallites while X-ray diffraction gives the vertical size of the crystallites because of the penetration of the X-ray into the films. The micrograph of the doped film is similar to that of the undoped one, which is consistent with the X-ray diffraction results.

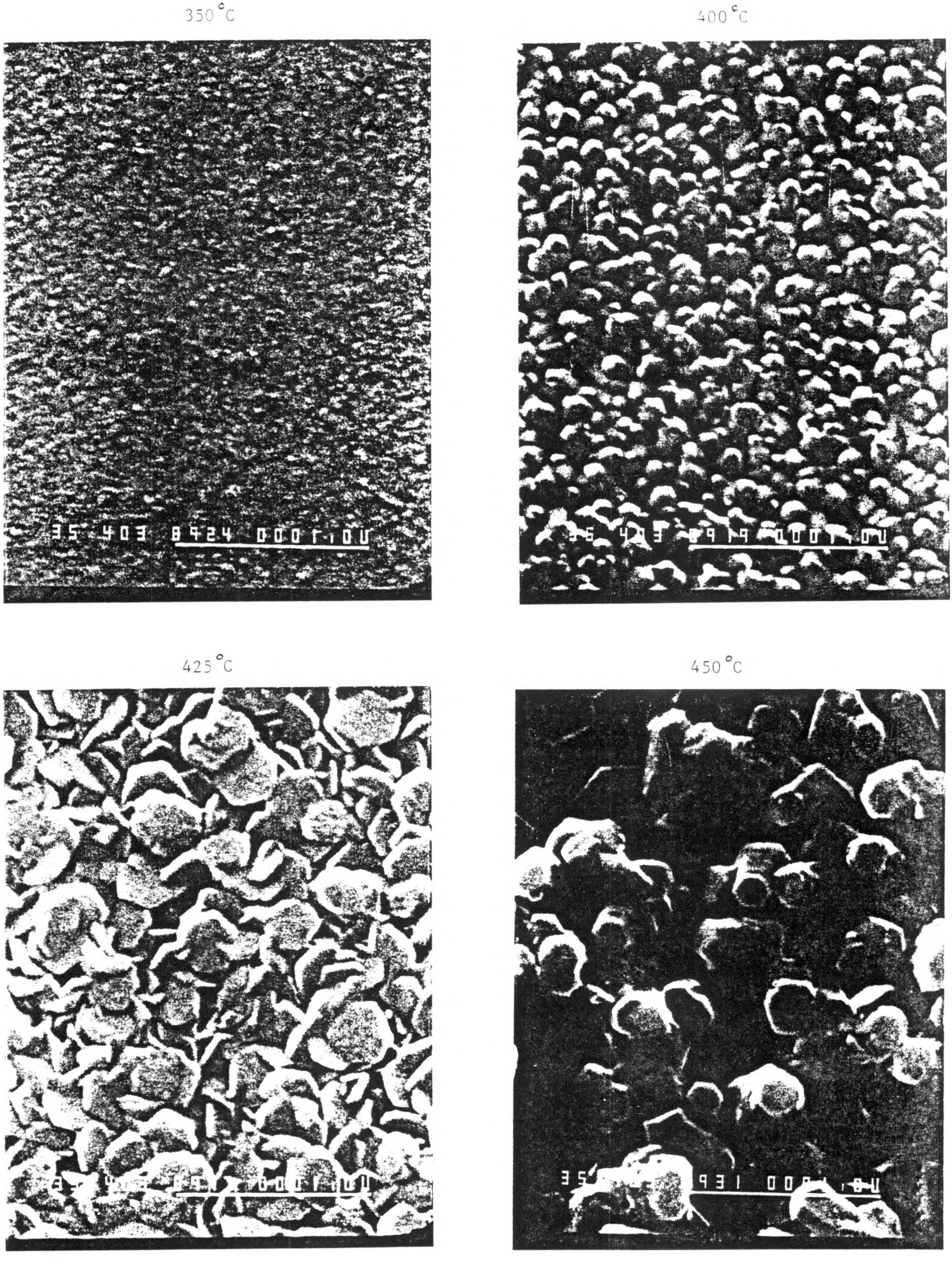

Fig.9. Scanning electron micrographs for films deposited at different temperatures.

5.3.3 Electrical characterization

After the doped films were deposited, their sheet resistance was measured by using a Veeco Fpp-100 four point probe. From the sheet resistances and the thicknesses of the films, which were determined from visible reflectance data, the conductivity can be determined. Figure 26 shows the conductivity as a function of film position on the substrate. This position dependence of film conductivity may result from the non-uniform fluorine distribution in the film. We find that fluorine is a n-type dopant for ZnO, which increases the free electron concentrations and film conductivity. However, the doping efficiency depends on the replacement of oxygen atoms by fluorine inside the ZnO crystal structure. A small amount of the insulating compound ZnF_2 can be produced from excess fluorine atoms inside the film and the excess fluorine therefore is no longer a dopant for the films with a high fluorine content. The best fluorine concentration for doped film at 400°C can be found from Figure 27, to be about 0.5%.

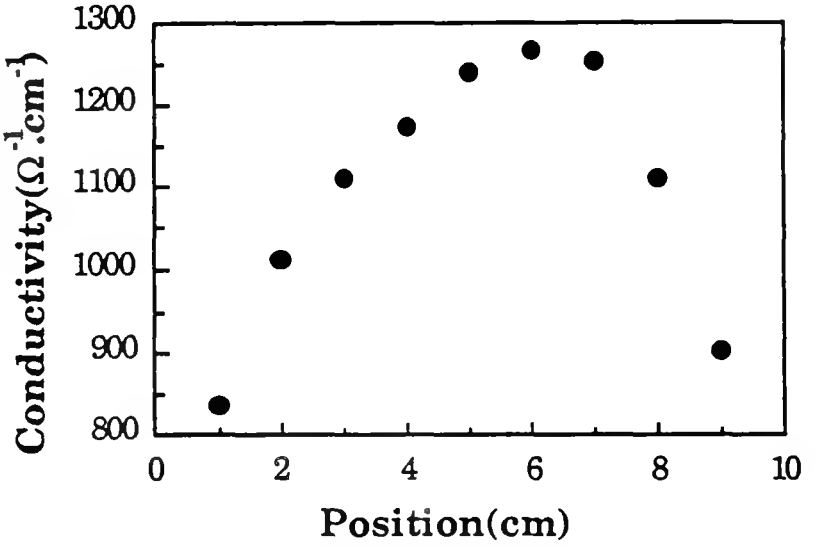

Fig. 26. Conductivity as a function of position on the substrate. The deposition temperature is 400°C and the dopant gas concentration is 5.79×10^{-5} mol·l^{-1}.

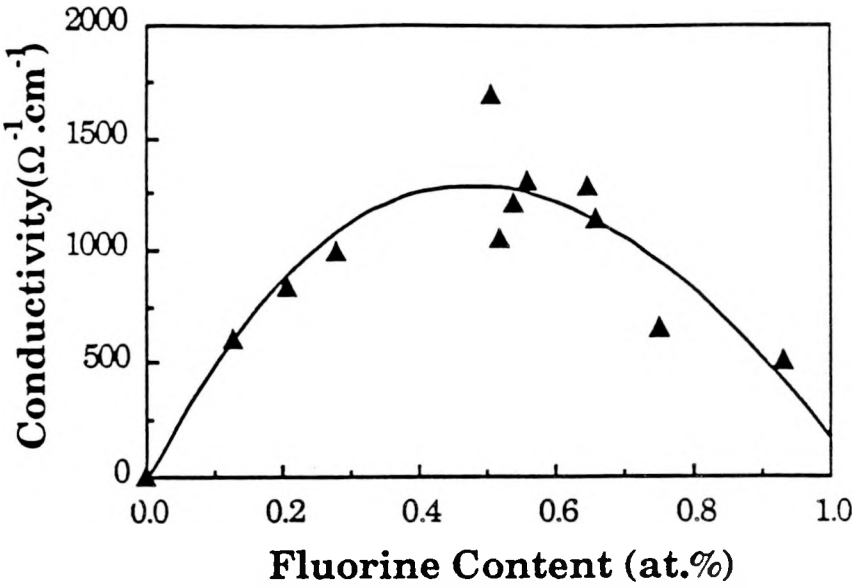

Fig. 27. Conductivity as a function of fluorine content for fluorine-doped zinc oxide films deposited at 400°C.

The deposition temperature can have a strong influence on both the break up of the dopant gas and the movement of dopant atoms to the correct positions. The doping efficiency η_{DE}, which is defined as the ratio of the carrier concentration to the fluorine atom concentration, can be calculated from the electron concentration, the fluorine percentage and the ZnO density, which is taken to be the same as the bulk density 5.606 gram/cm^3. The doping efficiency gives the fraction of the fluorine atoms that are electrically active in the film. We find that η_{DE} increases as the temperature becomes higher. At low deposition temperatures, some fluorine atoms do not occupy the correct positions (oxygen sites) inside the ZnO crystals and so they do not contribute free electrons to the film or increase film conductivity. These extra fluorine atoms may play an important role in introducing new states in the band gap and may degrade the film properties by providing more scattering centers.

The measured Hall coefficient can be used to calculate the free electron density of the film. As more and more fluorine is incorporated into the film the electron density first increases and then decreases, as shown in figure 28. Comparing figure 27 and figure 28, it is obvious that the films with best fluorine content have both highest conductivity and highest free electron density. The film mobility can be determined from the Hall coefficient and the conductivity of the film following a simple formula:

$$\mu_H = R_H \sigma \qquad (1)$$

Whereas lightly doped single crystal ZnO mobilities are typically 200 - 250 cm^2/V-s, the mobilities for the polycrystalline doped ZnO varied from 10 - 35 cm^2/V-s. These lower values may be expected because the deposited ZnO film is polycrystalline and the carriers undergo scattering by the grain boundaries. High fluorine concentrations will also increase the scattering and therefore decrease the mobilities. This phenomenon can be seen in Figure 29, which shows mobility as a function of fluorine concentration for films deposited at 400°C. The temperature dependence of the doping efficiency, film conductivity, electron density and mobility and also the corresponding optical analysis results are listed in table 6.

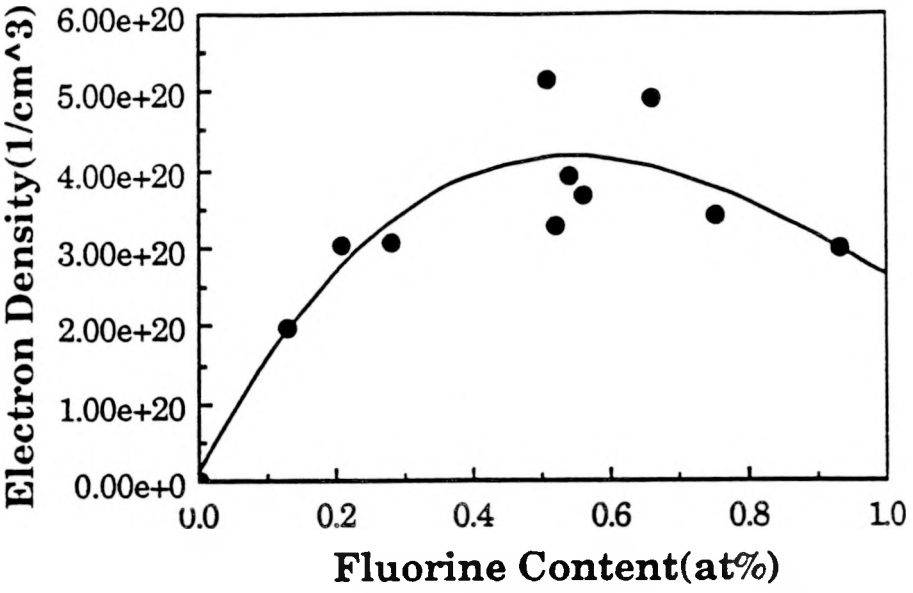

Fig. 28. Free electron density of fluorine doped ZnO films, determined from the measured Hall coefficients. The deposition temperature is 400°C.

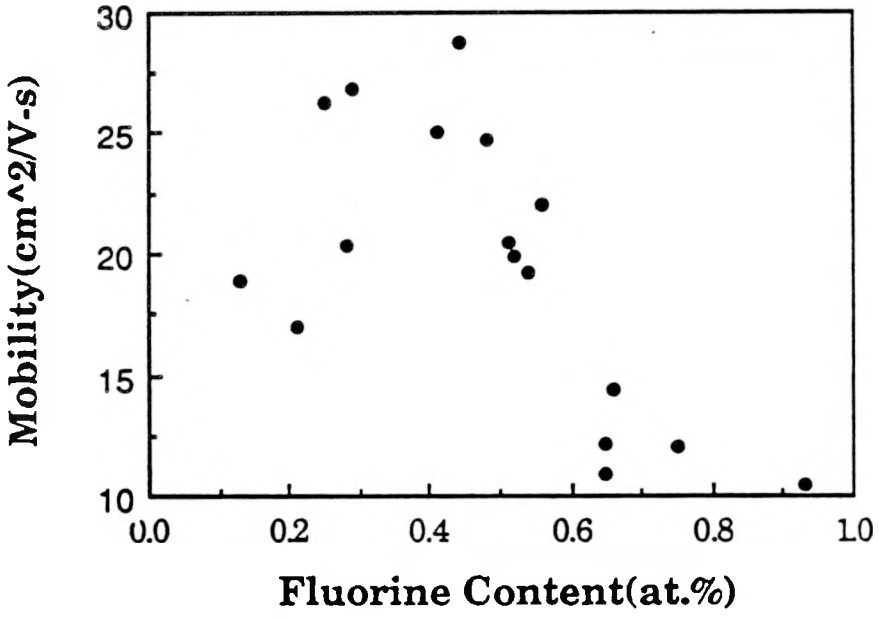

Fig. 29. Electron mobility as a function of fluorine concentration for ZnO:F films deposited at 400°C.

Table 6. The doping efficiency, film conductivity, mobility and carrier concentration determined from Hall coefficient and optical analysis.

		Optical analysis			Hall Coefficient		
Sample %	η_{DE} $1/cm^3$	n_e $\Omega^{-1}.cm^{-1}$	σ $cm^2/V\text{-}s$	μ $1/cm^3$	n_e $\Omega^{-1}.cm^{-1}$	σ $cm^2/V\text{-}s$	μ

A	65.3	2.81×10^{20}	1.31×10^{3}	29.1	3.36×10^{20}	0.93×10^{3}	17.3
B	76.3	2.72×10^{20}	1.45×10^{3}	33.4	3.67×10^{20}	1.35×10^{3}	23.0
C	96.7	2.44×10^{20}	1.32×10^{3}	33.9	3.85×10^{20}	1.53×10^{3}	24.7
D	84.9	2.70×10^{20}	1.39×10^{3}	32.1	2.96×10^{20}	1.41×10^{3}	29.8
E	96.4	1.83×10^{20}	0.99×10^{3}	33.9	2.00×10^{20}	1.15×10^{3}	35.9

5.3.4 Optical Measurement

Infrared reflectance spectra were measured on a Nicolet model 7199 Fourier transform spectrometer with a relative reflection attachment. The reflection standard is a gold mirror which has a known infrared reflectance spectra. The measured infrared reflectance of the doped film was corrected with respect to the spectra of the gold mirror before optical modeling. The near ultraviolet, visible and near infrared spectra were obtained with a Varian 2390 spectrophotometer using an integrating sphere detector which could measure both total and diffuse components of the reflectance and transmittance. The reflection standard for the visible and near infrared spectra is a mirror painted with barium sulfate which is known to have a high reflectance in the visible range. Fig. 30 shows some typical diffuse spectra, which show a characteristic increase in intensity for shorter (bluer) wavelengths.

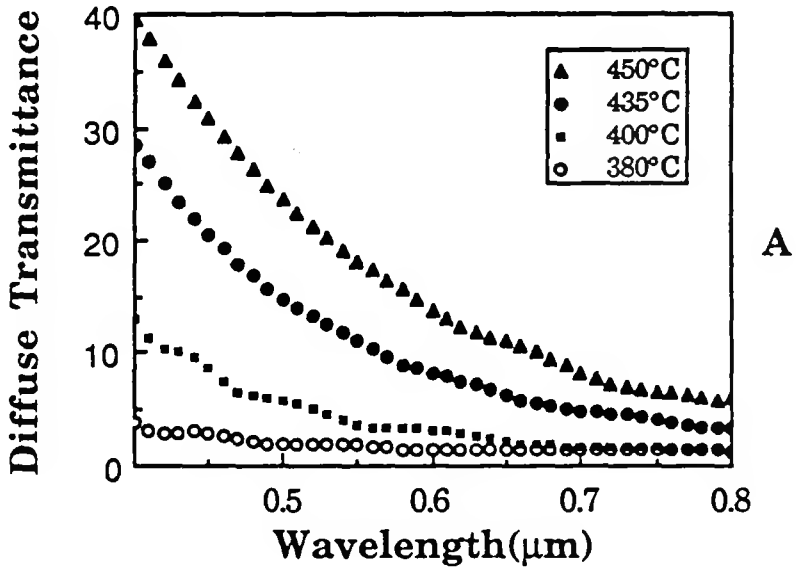

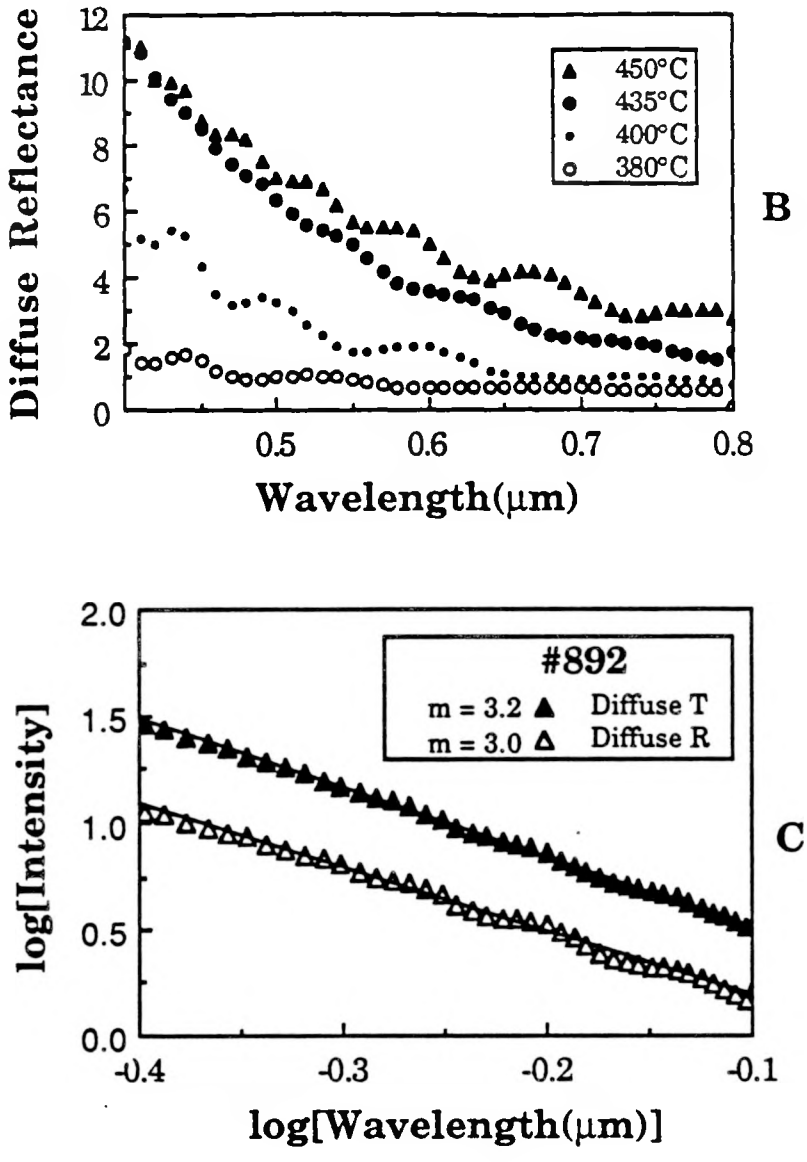

Fig. 30. A and B shows the diffuse reflection and transmission as a function of wavelength for samples deposited at different temperatures. The concentrations of DEZ, ethanol and hexafluoropene are 2.60×10^{-5} mol·l^{-1}, 1.54×10^{-3} mol·l^{-1} and 5.79×10^{-5} mol·l^{-1}. C is a plot of logarithm intensity vs logarithm wavelength for a sample deposited at 435°C and two almost parallel straightlines can be obtained. The average m is 3.1 and the T_0 and f_r determined from the figure are 0.4 and 1.8.

The free electrons inside the doped ZnO films modified some of their properties. In the infrared range, the films behave like metals and they have high reflectance and low transmittance. In the visible range, however, they are highly transparent and their reflectance spectra look like those of dielectrics. The crossover between those two type of behavior is the so-called plasma wavelength which will move to shorter wavelength as the free electron density in the film increases. Some applications of these semiconductor films use this peculiar change from metal-like to insulator-like optical properties. Figure 31 shows the spectrum of a doped film deposited at 400°C.

5.4 Theoretical model and data fitting

The resistivity network method used in this work is mainly due to Proscia who has successfully applied it to fluorine doped tin oxide film [38]. Spectral reflectance and transmittance data, such as those shown in figure 31, can be used to derive the complex dielectric function $\varepsilon = \varepsilon_1 + i\varepsilon_2$, or equivalently the complex reflective index $N = n - ik$. These functions contain useful information about optical properties of the film and are needed for both reliable comparison with theory and for optimizing the performance of the coating. Owing to the experimental uncertainties in the determination of the film's reflectance and transmittance, ε_1 and ε_2 are not calculated from Fresnel's equation at each wavelength, but are obtained by minimizing the difference between the experimental spectra and the model spectra.

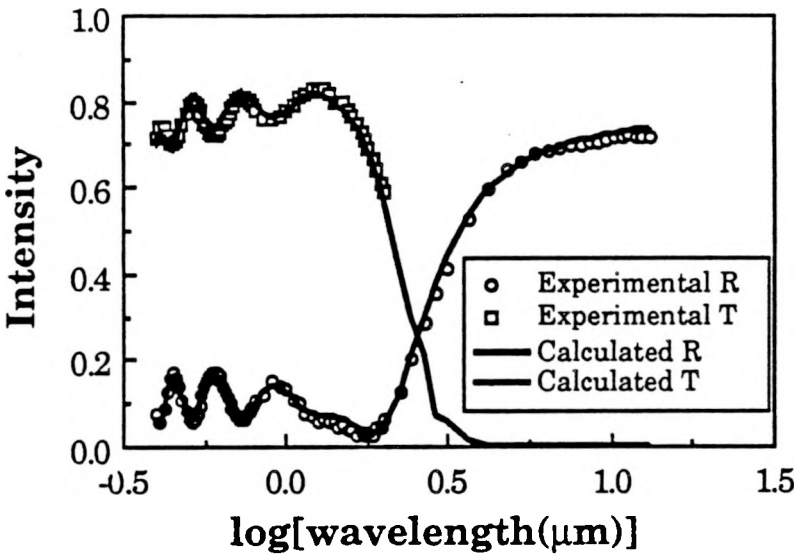

Fig. 31. Typical experimental and calculated specular spectra. The film was deposited at 400°C from DEZ, Ethanol and hexafluoropropene with concentrations of 2.60×10^{-5} mol·l^{-1}, 1.54×10^{-3} mol·l^{-1} and 5.79×10^{-5} mol·l^{-1}. The calculated parameters are: film thickness = 0.39μm, electron density n = 2.47×10^{20}cm^{-3}, $f_1^{\parallel}$ =10.1%, $f_1^{\perp}$ = 3.1%, A = 94.3, λ_b = 2.44μm, p = -2.41, two Urbach parameters U = 0.41μm^{-1} and $\alpha = 1.65\times10^{-3}$eV^{-1}, conductivity $\sigma = 8.65\times10^{2}\Omega^{-1}$·cm^{-1} and mobility μ = 21.9cm^2/V-s. The electron density, conductivity and mobility determined from Hall coeffieient are 3.05×10^{20}cm^{-3}, $8.30\times10^{2}\Omega^{-1}$·cm^{-1} and 17.0cm^2/V-s.

The most important contributions to the dielectric function come from the interaction of electromagnetic radiation with free carriers, ionized impurities [37] and grain boundaries [38]. The classical Drude theory is a free electron approximation and the interactions between electrons are neglected. This theory also assumes a constant scattering frequency which is defined as the probability per unit time that a carrier undergoes a collision. The frequency dependence dielectric function $\varepsilon(\omega)$ can be derived to be

$$\varepsilon(\omega) = \varepsilon_\infty + \frac{i}{\varepsilon_0 \omega \rho(\omega)} \qquad (2)$$

Here ε_∞ is the high frequency dielectric constant and equal to 3.85 for ZnO [22] and ε_0 is the permitivity of free space. The dynamic resistivity $\rho(\omega)$ is given by

$$\rho(\omega) = \frac{\omega_\tau}{\varepsilon_0 \omega_p^2} + \frac{i\omega}{\varepsilon_0 \omega_p^2} \qquad (3)$$

where $\omega_p^2 = \frac{ne^2}{\varepsilon_0 m^*}$ is the plasma frequency and is evaluated from the condition $\mathrm{Re}(\varepsilon(\omega_p)) = 0$, ω_τ is the constant Drude scattering frequency. m^* is the effective mass of electrons in the conduction band and is taken to be $0.280m_e$[22], and m_e and e are the electron mass and charge. When ω_p is measured, the free electron density n_e of the film can be calculated from the expression for ω_p^2.

In the resistivity network model of grain boundary scattering the fact that the film is polycrystalline and the distribution of the scatters is inhomogeneous has been taken into account and the resistivity in expression (2) will be replaced by an effective dynamical resistivity ρ_{eff} which can be derived from the electrical network analysis of the polycrystalline films [38]:

$$\rho_{eff} = \frac{(f_1^{\perp}\rho_1 + f_2^{\perp}\rho_2)\rho_2}{f_2^{\parallel}\rho_1 + f_1^{\parallel}\rho_2} \qquad (4)$$

Here $f_1^{\parallel}$ and $f_1^{\perp}$ are the volume fraction for electric field parallel and perpendicular to the grains and $f_2^{\parallel} = 1 - f_1^{\parallel}$ and $f_2^{\perp} = 1 - f_1^{\perp}$; ρ_1 and ρ_2 are the complex resistivity of the grains and grain boundaries. $f_1^{\parallel}$ and $f_1^{\perp}$ are not derived by any geometric arguments, but were varied independently in the computation to account for the effects of anisotropy, varying grain size and crystalline orientation and also other scattering mechanisms which are neglected in the computer program.

The determination of ρ_1 and ρ_2 requires specification of the scattering mechanism. The ionized impurity scattering model, which plays an important role in the grains. assumes a uniform distribution of scatters and the expression for dynamical resistivity can be obtained from energy loss considerations and can be written as [37]:

$$\rho(\omega) = i\frac{Z^2 N_i}{6\pi^2 \varepsilon_0 n^2 \omega} \int_0^\infty k^2 dk \left(\frac{1}{\varepsilon_L(k,\omega)} - \frac{1}{\varepsilon_L(k,0)} \right) - i\frac{\omega}{\varepsilon_0 \omega_p^2} \qquad (5)$$

Here Z is the charge of the ionized scattering centers and taken to be 1 for fluorine doped ZnO films. N_i is the concentration of scatters and n is the carrier concentration. These two quantities are forced to be equal in the computations. $\varepsilon_L(k,\omega)$ is the Lindehard dielectric function and has been given elsewhere [22]. $\varepsilon_L(k,0)$ is the static dielectric function. The effects described in

equation (4) and (5) can be recast into a Drude-like form by allowing a dispersive scattering frequency ω_τ which is given by $\omega_\tau = \varepsilon_0 \omega_p^2 \mathrm{Real}(\rho_{eff})$.

The scattering mechanism within the grains is assumed to be ionized impurity scattering and the resistivity ρ_1 of the grains will be given by equation (5). The integration in (5) was solved numerically at long wavelength and the real part of the resistivity was calculated and assumed to be constant towards short wavelength until it crosses a power law dependence observed at wavelengths shorter than the plasma wavelength. This power law dependence is given by

$$\rho(\omega) = \frac{Z^2 N_i e^2 m^{1/2}}{6\pi(\varepsilon_L(0)\varepsilon_0)^2 n h^{1/2}} \omega^{-3/2} \qquad (6)$$

The imaginary part of the resistivity was assumed to follow the usual dependence on frequency governed by Drude theory. This has been shown to be a good approximation because the last term in (5) is dominated by Drude component [22].

The grain boundary resistivity ρ_2 is constructed by assuming its real part in the long wavelength is a factor of A larger than that in the grains and has a different power law dependence on frequency in the short wavelength range. The imaginary part of ρ_2 is assumed to be equal to that of the grains. The break wavelength λ_b is defined as the wavelength at which the grain boundary scattering frequency changes from constant to an asymptotic power law relation. The power **p** of the scattering frequency on the grain boundary and λ_b were allowed to vary to give the best fit between theory and experiment.

The high frequency dielectric constant also has some dispersion in the blue and uv regions of the spectrum. It can be estimated by a single damped Lorentz oscillator and its real part is given by the following expression [38]:

$$\varepsilon_\infty = p_1 + \frac{p_2\left(1 - \left(\frac{p_3}{\lambda}\right)^2\right)}{\left(1 - \left(\frac{p_3}{\lambda}\right)^2\right)^2 + p_4\left(\frac{p_3}{\lambda}\right)^2} \qquad (7)$$

Here p_1, p_2, p_3, and p_4 are parameters determined from the optical analysis. The effect of this dispersion can be observed in the reflectance spectrum as an anomalously high interference maximum in the 400 - 450 nm range.

Some of the visible absorption is due to "tails" of the band-to-band transitions. Its influence on the dielectric function is additive and it can be described empirically by an Urbach-like equation [40]:

$$\varepsilon_{\text{band tail}} = iU\lambda e^{\alpha\hbar\omega} \qquad (8)$$

Here U and α are parameters determined in the optical data fitting.

Although the dielectric function could be constructed as described above, the theoretical reflectance and transmittance could not be calculated accurately from Fresnel's equation because the film surface usually is not smooth and a diffuse component must be included for comparison between experiment and theory. The surface roughness has the effects of lowering the total reflection of the

film in the visible range, increasing the transmission and decreasing the magnitude of the interference oscillations. It can be simulated by a gradient in the dielectric function [39]. The specularly reflected and transmitted beams are also diminished by the loss of the diffusely scattered components and the incident light will be attenuated by a factor:

$$1 - S_c = 1 - R_d - T_d \qquad (9)$$

where $1 - S_c$ is the attenuation factor, R_d is the diffuse reflectance and T_d is the diffuse transmittance. The diffuse components gradually vanish as the wavelength moves to near infrared and infrared range. In solar cell applications the diffuse components are useful in improving cell performance. The overall cell efficiency was found to increase rapidly as the diffuse transmission increased to about 5%. The maximum efficiency occurs at the best compromise between optimizing light trapping and minimizing other losses [41]. The measured R_d and T_d can be parameterized via the common power law expressions:

$$T_d = \frac{T_0}{\lambda^m} \qquad R_d = f_r T_d \qquad (10)$$

These three parameters T_0, m and f_r will be determined experimentally. Figure 30a and 30b showed the deposition temperature dependence of the diffuse reflectance and transmittance in the visible range. As the temperature increases, the films become rougher and both diffuse transmittance and reflectance increase. The oscillations in the spectra are due to the light interference by the thin films. Figure 30c shows that two almost straight lines with slope of 3.2 and 3.0 can be obtained when logarithms of diffuse transmittance and reflectance are plotted vs logarithm of wavelength. The determined exponent m for samples deposited above 400°C lies between the limiting values 2 and 4, which correspond to the Mie and Rayleigh scattering limits, respectively. The m value for the sample deposited at 380°C is about 1.6. This deviation from the theoretical range might result from the uncertainty in the determination of the diffuse component because of its smallness at this temperature. Table 7 lists some of the parameters obtained from optical analysis.

Table 7. Some parameters obtained from optical analysis. The samples are the same as those in table 5. Included are film thickness, parallel component $f_1^{\parallel}$, perpendicular component $f_1^{\perp}$, amplitude factor A, break wavelength λ_b, scattering power law in the grain boundary p, two Urbach parameters U and α and the surface roughness Rf as a percentage of the film thickness. The fitting error varies from 1.5% to 3.5%.

Sample	Thickness	$f_1^{\parallel}$	$f_1^{\perp}$	A	λ_b	p	U	α	Rf
μm	%	%		μm		μm^{-1}	eV^{-1}	%	
A	0.347	2.24	3.52	70.6	2.30	-2.12	1.92	5.34×10^{-3}	0.48
B	0.366	8.64	2.16	8.60	2.79	-0.81	1.41	4.74×10^{-3}	1.18
C	0.492	26.8	10.5	8.80	2.60	-1.47	1.72	5.87×10^{-3}	0.76
D	0.360	5.93	7.42	25.9	2.56	-4.36	0.891	2.00×10^{-3}	1.68
E	0.483	11.4	10.8	14.6	2.89	-2.91	2.00	2.84×10^{-3}	1.04

The scattering frequency γ was obtained from optical analysis at wavelengths shorter than 12 microns. If it is assumed to be constant at longer wavelengths, then it can be used to calculate the the DC conductivity σ by the following formula:

$$\sigma = \frac{n_e e^2}{m^* \gamma} \qquad (11)$$

where electron density n_e can be obtained from the plasma frequency ω_p. Considering that the polar optical phonons in the ZnO film have an influence on the dielectric functions at very long wavelength (larger than 12μm) and this effect is not taken into account in our calculations, there is reasonable agreement (shown in Table 6) between the measured DC conductivities and the values extrapolated from the optical analysis. The mobility can be obtained from:

$$\mu = \frac{\sigma}{n_e e} \qquad (12)$$

The carrier concentrations, conductivities and mobilities determined from infrared spectra generally agree well with those determined from the Hall coefficient and resistance measurements. (See Table 6)

The experimental and calculated spectra from 0.4 to 12μm were shown in figure 31. The sample was deposited at 400°C on soda lime glass from DEZ, ethanol and hexafluoropropene with concentrations of 2.6×10^{-5}mol/l, 1.54×10^{-3}mol/l and 5.79×10^{-5}mol/l. This sample was taken from the center of the substrate and was not the most conductive sample. Its thickness from optical analysis is 0.39μm and its composition determined from microprobe analysis is Zn : 50.8at.%, O : 49.0at.% , F : 0.21at%. The film conductivity, electron density and mobility obtained from optical analysis are $8.65 \times 10^2\ \Omega^{-1}\cdot cm^{-1}$, 2.47×10^{20}1/cm^3 and 21.9cm^2/V-s, which can be compared with those obtained from Hall coefficient, $8.30 \times 10^2 \Omega^{-1}\cdot cm^{-1}$, 3.05×10^{20}1/cm^3 and 17.0cm^2/V-s. The maxium fitting error is 1.8% and the agreement between experimental and theoretical spectra is quite good.

5.5 Conclusions

Fluorine-doped zinc oxide is a promising new transparent conducting material which has been prepared from DEZ, ethanol and hexafluoropropene in the temperature range from 375°C to 450°C at atmospheric pressure. The film thicknesses and refractive indices were determined from ellipsometry for thicknesses between 500Å and 1900Å. The thicknesses of the thicker films were obtained from visible reflectance data fitted to a theoretical optical model. The refractive index was found to depend on film thickness and the deposition temperature and this variation can be explained by a density gradient along the direction perpendicular to the substrate. The film growth rate was found to depend linearly on DEZ concentration in the presence of excess ethanol. Electron microprobe shows that the deposited film has a non-uniform fluorine distribution along the gas flow. Film properties depend on which part of the substrate the samples were taken from, and we have chosen samples from the center and from the most conductive parts. X-ray diffraction and SEM reveal that the film is oriented with c-axis perpendicular to the substrate and that the grain size increases with the deposition temperature.

The doped film is highly conductive and has excellent stability. Optical measurements show that the film has high transmission in the visible range and high reflection in the infrared. Hall coefficient measurements were taken to determine the electron density in the film. The mobility has been obtained from Hall coefficient and the resistivity measurements. The fluorine content of about 0.5 atomic percent gives the highest electron density, conductivity and mobility for films

deposited at 400°C. The film becomes rougher and the doping efficiency becomes higher at higher deposition temperatures.

The optical properties of the film are consistent with a Drude-like behavior altered by the incorporation of scattering by ionized impurities and a simple resistive network model of grain boundary scattering. Grain boundary scattering seems to be an important mechanism in the limit of film d.c. conductivity and infrared reflectance. The band gap absorption was modeled by an empirical Urbach-like equation. Film roughness was treated according to the method by Szczyrbowski which describes the attenuation of the interference oscillations in the visible reflectance spectra. The large-scale CVD at atmospheric pressure is able to produce inexpensively doped ZnO film with promising structures for efficient light-trapping and good electric and optical properties for transparent electrodes in solar cells. Other possible applications include transparent conducting electrodes for liquid crystal or electrochromic displays.

Appendix A: TITANIUM NITRIDE THIN FILMS: PROPERTIES AND APCVD SYNTHESIS USING ORGANOMETALLIC PRECURSORS

RENAUD M. FIX, ROY G. GORDON AND DAVID M. HOFFMAN
Harvard University, Department of Chemistry, 12 Oxford Street, Cambridge, MA 02138

ABSTRACT

A novel process for the low temperature synthesis of titanium nitride thin films by APCVD is described. TiN coatings containing less than one atom percent of carbon and oxygen were deposited at 200 °C on silicon, vitreous carbon, glass, stainless steel and plastic substrates using $Ti(NMe_2)_4$ and ammonia gas as precursors. The films were characterized by Rutherford backscattering spectrometry and X-ray photoelectron spectroscopy.

INTRODUCTION

Titanium nitride thin films have numerous potential applications because they are extremely hard, high melting (ca. 3000 °C), chemically inert, electrically conducting (better than titanium metal itself) and have optical properties similar to those of gold.[1] High quality titanium nitride coatings can be prepared by atmospheric pressure chemical vapor deposition (APCVD) using titanium tetrachloride, nitrogen and hydrogen at temperatures around 1000 °C (eq 1).[2]

$$TiCl_4 + 1/2N_2 + 2H_2 \xrightarrow{900\text{-}1000\ ^\circ C} TiN + 4HCl \qquad (1)$$

The temperature of this deposition process restricts its use to refractory substrates such as tungsten carbide. In another APCVD process, Gordon and Kurtz have shown that with titanium tetrachloride and ammonia precursors the deposition of titanium nitride thin films occurs under significantly milder conditions (eq 2), thereby allowing the use of thermally sensitive substrates such as low sodium glass and silicon. The temperature required for the Gordon-Kurtz process, however, is still too high for delicate substrates such as aluminum-metallized silicon chips, amorphous silicon solar cells and plastics. Also, the corrosive HCl by-product from reaction 2 is undesirable from a technological standpoint, and, furthermore, traces of chloride in the films prepared using this system apparently cause adhesion problems on stainless steel substrates.[3]

$$6TiCl_4 + 8NH_3 \xrightarrow{500\text{-}700\ ^\circ C} 6TiN + 24HCl + N_2 \qquad (2)$$

It is clear that if all applications of TiN films are to be realized, then systems that permit still lower deposition temperatures must be developed. In this regard, Bradley and co-workers showed several years ago that, in solution, $Ti(NR_2)_4$ complexes undergo transamination reactions under very mild conditions (eq 3).[4] More recently, polymeric titanium imides were transaminated with NH_3 and pyrolized to form TiN in the form of a porous solid ceramic.[5] Based on these studies, the possibility of using $Ti(NR_2)_4$ compounds and ammonia as precursors for the low temperature

$$Ti(NR_2)_4 \xrightarrow{\text{excess } HNR'_2} Ti(NR'_2)_4 + 4HNR_2 \qquad (3)$$

preparation of TiN films in a APCVD process analogous to Gordon and Kurtz's appeared tenable (eq 4).

$$Ti(NR_2)_4 \xrightarrow{\text{excess } NH_3} TiN + \text{volatile organic products} \quad (4)$$

Herein is presented a description of the successful APCVD synthesis of high quality TiN coatings by use of the dual precursor system tetrakis(dimethylamido)titanium, $Ti(NMe_2)_4$, and ammonia.

EXPERIMENTAL SECTION

The compounds $Ti(NMe_2)_4$ and $Ti(NEt_2)_4$ were synthesized as described by Bradley and Thomas.[4] We have previously reported the preparation of $Ti(NMe_2)_3(t\text{-Bu})$.[6]

Depositions were carried out in a atmospheric-pressure laminar-flow rectangular glass reactor heated from below, which has been previously described.[3] Ultra high purity helium, passed through a gettering furnace followed by a Nanochem gas purifier (Model L-50 t), was used as carrier gas for the titanium-containing precursor and as diluent for the ammonia. Electronic grade ammonia, obtained from Matheson, was purified using a Nanochem resin. The CVD system, loaded with the substrates, was purged for at least 2 hours before each deposition. Under these conditions, analyses of the helium outflow showed that it contained less than 0.1 ppm O_2 and H_2O. During the deposition process, helium was passed through a stainless steel bubbler containing the titanium precursor, and this mixture then flowed through a 1 mm i.d. delivery line to the reaction chamber. Approximately 2 cm before this delivery line entered the reaction chamber, the $Ti(NMe_2)_4$/He mixture was combined with ammonia gas diluted in helium (10%). The combined mixtures then flowed over the hot substrate. Outflow from the reaction chamber exited to an oil bubbler, which prevented back flow of air into the reaction chamber. After each deposition the films were allowed to cool slowly in the reactor under a flow of helium.

Silicon substrates were cleaned by immersion in H_2O_2:H_2SO_4 (1:4) for 10 minutes and then dilute HF until hydrophobic. Deionized water was used for final rinsings. The vitreous carbon and boron substrates, which were obtained from Atomergic Chemetals Corp., were degreased in $C_2F_3Cl_3$. The glass substrates were either Corning 7059 low sodium glass or normal borosilicate glass. They were etched for 1 minute in HF/HNO_3 (1:10) and then rinsed with deionized water.

Rutherford backscattering (RBS) analyses (General Ionics Model 4117) were performed using a beam of He^+ of energy 2.0 MeV for films deposited on silicon and vitreous carbon and 1.8 MeV for films deposited on boron. (It should be noted that boron gives a nuclear reaction with He^+ at a nuclear resonance of 2.06 MeV).[7] X-ray photoelectron spectroscopy (XPS) was carried out using a Surface Science Lab SSX-100 system equipped with a 3 keV Ar^+ sputter gun. The electron-energy analyzer was calibrated to the Au $4f_{7/2}$ line at 84 eV. XP spectra were collected in the unscanned mode by using the monochromatized Al K_α excitation with a spot size 600 μm and the electron-energy analyzer set for a pass energy of 150 eV. The experimental detector width is 18.6 eV in this configuration. The base pressure was 10^{-7} torr with the Ar^+ gun on. The transmission electron micrographs and electron diffraction patterns were obtained on a Philips EM420T scanning transmission electron microscope.

RESULTS AND DISCUSSION

Depositions at temperatures from 100 to 400 °C were successfully carried out on silicon wafers, normal and low sodium glass, stainless steel, vitreous carbon and boron substrates using $Ti(NMe_2)_4$ and NH_3 as precursors. A polyester film was also used as a substrate for depositions

below 200 °C. If the ammonia reactant is omitted from the process, no deposition is observed below 300 °C, and, at this temperature, only powdery deposits are obtained.[6] Growth rates, which ranged from 200 to 2000 Å/min, depended only on the vapor pressure of $Ti(NMe_2)_4$ and could be increased by simply preheating the carrier gas and precursor.

In general, the deposits were smooth, nonporous and mirror-like, with a gold color typical of TiN. The coatings adhered well (Scotch tape test) to all substrates. They resist scratching and abrasion and are chemically inert, except to hydrofluoric acid, in which they are readily dissolved.

The morphology of the films was examined by transmission electron microscopy (TEM) (e.g., Figure 1). The films are polycrystalline with very small crystallites (2-10 nm). Because the crystallites are small, a single crystal electron-diffraction pattern could not be obtained. The electron-diffraction ring patterns, however, are consistent with the powder diffraction of TiN (e.g., Figure 2).[8] Scanning electron micrographs of the films are featureless.

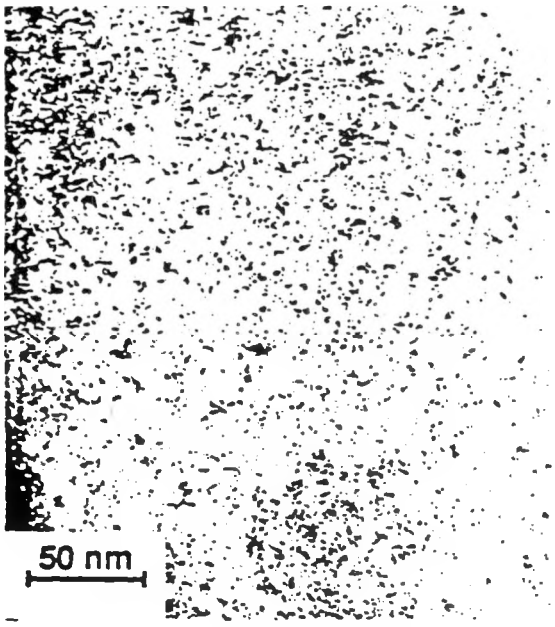

Figure 1: TEM of a TiN thin film deposited at 200 °C

Figure 2: TEM electron diffraction pattern for TiN deposited at 200 °C.

Film thicknesses and bulk compositions, including reliable light element contents, were readily obtained by RBS analyses of coatings deposited on boron substrates, wherein light element peaks are not obscured by any substrate background.[6] XPS depth profile data was also obtained in order to provide chemical bonding information and composition data complementary to the RBS results. According to the RBS data, films deposited below 300 °C had N/Ti ratios of approximately 1.1-1.2 and film thicknesses ranging from 500 to 2500 Å. Carbon contamination of the films, which arises from precursor decomposition (see below), was minor when depositions were carried out below 300 °C (Table). The binding energy of the carbon 1s XPS peak (282 eV) shows that the carbon is mostly titanium-bound.[9] Oxygen contamination was also small. The source of oxygen contamination in the films appears to be O_2 diffusion from the glass reactor; future work with stainless steel reactors should minimize this technical problem.

Table: Carbon content as a function of deposition temperature.

Deposition Temperature (°C)	C/Ti ratio
200	<0.02
250	0.05
300	0.09
350	0.11
400	0.11-0.2

Thus far, the highest purity films have been obtained at 200 °C. They contain less than 1 atom percent of carbon and oxygen (as determined by RBS; Figure 3). XP spectra (Figures 4 and 5) obtained for the same films reveal binding energies for Ti $2p_{3/2}$ and N 1s, 454.8 eV and 396.9 eV, respectively, that are consistent with TiN.[9] The amount of carbon and oxygen contamination as determined by XPS was consistent with the RBS data (<1 at %).

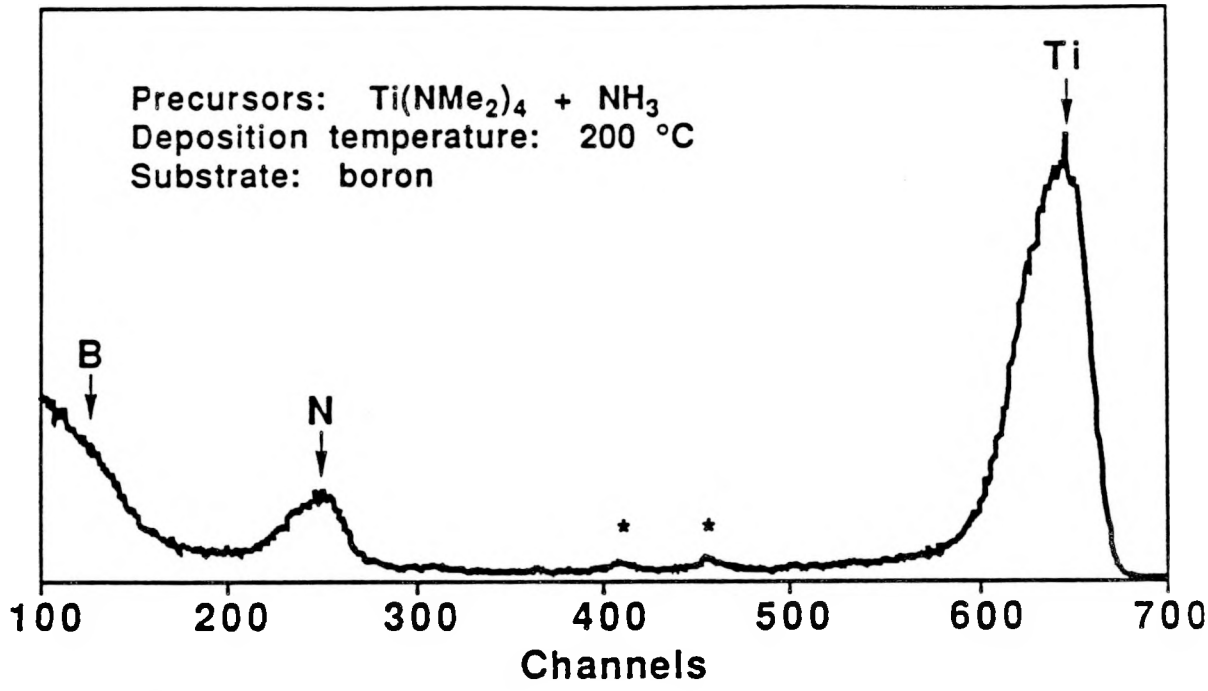

Figure 3: RBS spectrum for a TiN film deposited at 200 °C on boron. Beam: He^+, 1.8 MeV. The starred peaks are present in spectra obtained for clean boron substrates.

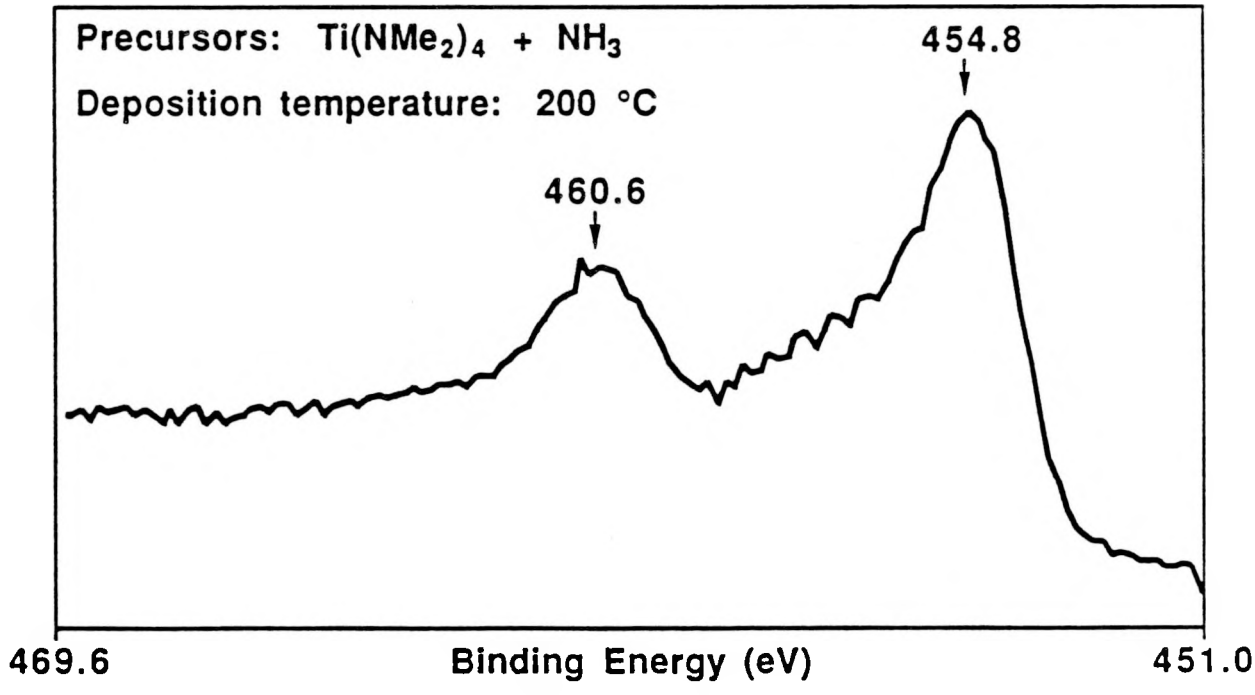

Figure 4: Ti 2p region of the XP spectrum.

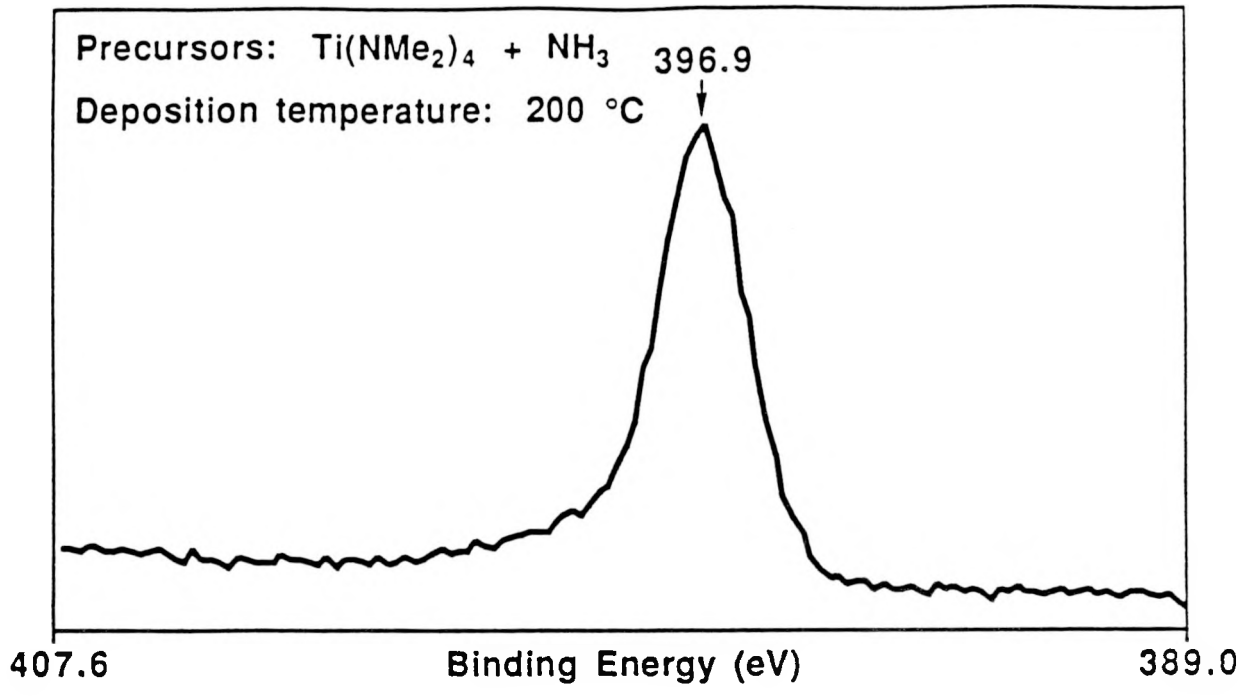

Figure 5: N 1s region of the XP spectrum.

Films of similar quality can be deposited within the same general temperature range using ammonia and other dialkylamido derivatives including $Ti(NEt_2)_4$ and $Ti(-t\text{-}Bu)(NMe_2)_3$. Growth rates using $Ti(NEt_2)_4$ and $Ti(-t\text{-}Bu)(NMe_2)_3$ as precursors are lower than when $Ti(NMe_2)_4$ is used, however, because the former are less volatile.

Mechanistic Rationalization

We can rationalize our results on the basis of well-known solution phase reaction pathways. In particular, based on Bradley's transamination reactions,[4] it is reasonable to suggest that the deposition process involves substitution of one or more dimethylamido ligands by NH_2 groups via reactions with ammonia, perhaps as an initial step or steps. The NH_2 substituted product could then intramolecularly eliminate an amine group (HNR_2, R = Me or H) via proton transfer or α-hydrogen activation involving a NH_2 ligand, thereby leaving an imido linkage (Ti=NH; Scheme). The proposed imido intermediate has some precedent in $[Ti(\mu\text{-}N\text{-}t\text{-}Bu)(NMe_2)_2]_2$, which is the solution product of the reaction of $Ti(NMe_2)_4$ with $t\text{-}BuNH_2$.[10] Another intramolecular proton or H-atom transfer and elimination of HNR_2, at some point in the process, would lead to a nitride linkage (Ti≡N).

Scheme

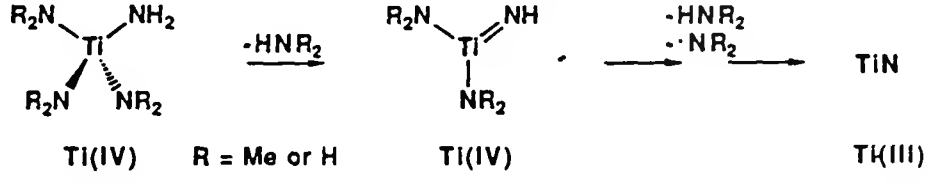

The oxidation state change that occurs for titanium during the deposition process (i.e., $Ti^{IV}(NMe_2)_4 \rightarrow Ti^{III}N$) may be accomplished via Ti-N homolytic bond cleavage, which would

produce an amido radical, $\cdot NH_2$ or $\cdot NR_2$, and the required Ti(III) center. Obviously, the proposed scheme is only one of many that would account for the preparation of TiN from our precursors.

The increased amount of carbon found in the films prepared at high temperatures can be explained as arising from intramolecular dimethylamido β-hydrogen activation, which only at the higher temperatures competes effectively with the chemistry described in the Scheme.[6, 11-14]

CONCLUSION

We have prepared high quality thin films of titanium nitride on a variety of substrates by APCVD using $Ti(NMe_2)_4$ and ammonia gas as precursors. The deposition temperature range is 100 to 400 °C, with the optimum range being 200 to 300 °C. The highest quality films, which contained less than one atom percent carbon and oxygen contamination, were deposited at 200 °C.

We are currently investigating the use of ammonia with other transition-metal amido precursors, including those of the Group IV, V and VI transition metals, in the APCVD process.

ACKNOWLEDGMENTS

We are grateful to the National Science Foundation (DMR-8802306) for support of this work. RMF thanks ICI Americas for a summer fellowship. We thank Yuan Z. Lu for his help in obtaining TEM data. Analyses of the thin films by TEM, XPS, and RBS were carried out at the facilities of the Harvard Materials Research Laboratory.

REFERENCES

1. Refractory Materials, edited by J. L. Margrave (Academic Press, New York, 1971).
2. W. Schintlmeister, O. Pacher, K. Pfaffinger, J. Electrochem. Soc. 123, 924 (1976).
3. S. R. Kurtz, R. G. Gordon, Thin Solid Films 140, 277 (1986).
4. D. C. Bradley, I. M. Thomas, J. Chem. Soc. 1960, 3857.
5. D. Seyferth, G. Mignani, J. Mater. Sci. Lett. 7, 487 (1988).
6. R. M. Fix, R. G. Gordon, D. M. Hoffman, submitted for publication.
7. L. L. Lee, Jr., J. P. Schiffer, Phys. Rev. 115, 160 (1959).
8. TiN: Index No. 38-1420. Powder Diffraction File, editor in chief: W. F. McClune (JCPDS International Centre for Diffraction Data, Swarthmore, PA 19081-2389, USA).
9. C. D. Wagner et al., Handbook of X-Ray Photoelectron Spectroscopy (Perkin-Elmer Corporation, Eden Prairie).
10. D. C. Bradley, E. G. Torrible, Can. J. Chem. 41, 134 (1963).
11. W. A. Nugent, D. W. Ovenall, S. J. Holmes, Organometallics 2, 161 (1983).
12. Y. Takahashi, N. Onoyama, Y. Ishikawa, S. Motojima, K. Sugiyama, Chem. Lett. 1978, 525.
13. K. J. Ahmed, M. H. Chisholm, K. Folting, J. C. Huffman, J. Am. Chem. Soc. 108, 989 (1986).
14. H. Bürger, H.-J. Neese, J. Organomet. Chem. 21, 381 (1970).

6.0 REFERENCES

1. Strickler, David, Ph.D. Thesis (Harvard University, 1989).

2. Dixon, J. R., "Electric-Susceptibility Mass of Free Carriers in Semiconductors", in Optical Properties of Solids, ed. Sol Nudelman and S. S. Mitra (Plenum Press, New York, 1969), pp. 61-83.

3. Hamberg, I. and Granqvist, C. G., J. Appl. Phys., Vol. 60, 1986, pp. R123-R159.

4. Köstlin, H.; Jost, R. and Lems, W., Phys. Stat. Sol. (a), Vol. 29, 1975, pp. 87-93.

5. Hamberg, I. and Granqvist, C. G., J. Appl. Phys., Vol. 60, 1986, pp. R146.

6. Gerlach, E. and Grosse, P., Festkörperprobleme (Advances in Solid State Physics), Vol. 17, 1977, pp. 157-193.

7. Hamberg, I. and Granqvist, C. G., Appl. Phys. Lett., Vol. 44, 1984, pp. 721-723.

8. Proscia, James W., Ph.D. Thesis (Harvard University, 1988).

9. van Daal, H. J., Solid State Commun., Vol. 6, 1968, pp. 5 .

10. Proscia, James W., Ph.D. Thesis (Harvard University, 1988).

11. Hamberg, I. and Granqvist, C. G., Appl. Opt., Vol. 24, 1985, pp. 1815-1819 .

12. Swanepoel, R., J. Phys. E: Sci. Instrum., Vol. 16, 1983, pp. 1214-1222 .

13. Manifacier, J. C.; Gasiot, J. and Fillard, J. P., J. Phys. E: Sci. Instr., Vol. 9, 1976, pp. 1002-1004 .

14. Szczyrbowski, J.; Schmalzbauer, K. and Hoffman, H., Thin Solid Films, Vol. 130, 1985, pp. 57-73 .

15. Swanepoel, R., J. Phys. E: Sci. Instr., Vol. 17, 1984, pp. 896-903 .

16. Szczyrbowski, J., J. Phys. D: Appl. Phys., Vol. 11, 1978, pp. 583-593 .

17. Swanepoel, R., J. Phys. E: Sci. Instrum., Vol. 16, 1983, pp. 1214-1222 .

18. Jarzebski, Z. M., and Marton, J. P., J. Electrochem. Soc., Vol. 123, 1976, pp. 299C-310C .

19. Ref. 1, Ch. 3, p. 59

20. Ref. 1, Ch. 3, p. 60

21. Burton, K. J.; Fonstad, C. G., and Dreyboldt, W., Phys. Rev. B, Vol. 4, 1971, pp. 4539.

22. Hamberg, I. and Granqvist,C. G., J. Appl. Phys., Vol. 60, 1986, pp. R123; Jin, Z. C.; Hamberg, I. and Granqvist, C. G., J. Appl. Phys., Vol. 64, 1988, pp. 5117.

23. Nanto, H. et al, J. Appl. Phys., Vol. 55, 1984, pp. 1029.

24. Minami, T.; Nanto, H.; Takata, S., Jpn. J. Appl. Phys., Vol. 24, 1985, pp. L605.

25. Qiu, S. N.; Qiu, C. X. and Shih, I., Solar Energy Mater., Vol. 15, 1987, pp. 261; Jin, Z. C.; Hamberg, I. and Granqvist, C. G., Appl. Phys. Lett., Vol. 51, 1987, pp. 149.

26. Vijayakumar, P. S. et al, U. S. Patent 4,751,149 (1988).

27. Lau, C. K.; Tiku, S. K. and Lakin, K. M., J. Electrochem. Soc., Vol. 127, 1980, pp. 1843.

28. Oda, S. et al, Jpn. J. Appl. Phys., Vol. 24, 1985, pp. 1607.

29. Webb, J. B. and Williams, D. F., Appl. Phys. Lett., Vol. 39, 1981, pp. 640.

30. Ito, K. and Nakazawa, T., Jpn. J. Appl. Phys., Vol. 22, 1983, pp. L245.

31. Watanabe, H., Jpn. J. Appl. Phys., Vol. 9, 1970, pp. 418.

32. Aranovich, J.; Ortiz, A. and Bube, R. H., J. Vac. Sci. Technol., Vol. 16, 1979, pp. 994.

33. Shealy, J. et al, J. Electrochem. Soc., Vol. 128, 1981, pp. 558.

34. Smith, F. T. J., Appl. Phys. Lett., Vol. 43, 1983, pp. 1108.

35. Gordon, R., unpublished results.

36. Cullity, B. D., Elements of X-ray Diffraction, 2nd edition (Addison-Wesley, Reading, MA, 1978).

37. Gerlach, E. and Grosse, P., Festkörperprobleme, Vol. 17, 1977, pp. 157; Gerlach, E., J. Phys. C: Solid State Phys., Vol. 19, 1986, pp. 4585.

38. Proscia, J., Ph.D. Thesis: (Harvard University, 1988).

39. Szczyrbowski, J.; Schmalzbauer, K. and Hoffmann, H., Thin Solid Films, Vol. 130, 1985, pp. 57.

40. Hamberg, I. and Granqvist, C. G., Appl. Opt., Vol. 24, 1985, pp. 1815.

41. Gordon, R. G., Proscia, J., Ellis, F. B. Jr. and Delahoy, A. E., Solar Energy Materials, Vol. 18, 1989, pp. 263.

Document Control Page	1. SERI Report No. SERI/TP-211-3666	2. NTIS Accession No. DE90000319	3. Recipient's Accession No.

4. Title and Subtitle
Charterization and Comparison of Optically Transparent Conducting Films, Final Subcontract Report

5. Publication Date
March 1990

6.

7. Author(s)
R.G. Gordon, Principal Investigator

8. Performing Organization Rept. No.

9. Performing Organization Name and Address
Harvard University
Cambridge, Massachussetts 02138

10. Project/Task/Work Unit No.

11. Contract (C) or Grant (G) No.
(C) XX-8-18148-1
(G)

12. Sponsoring Organization Name and Address
Solar Energy Research Institute
1617 Cole Boulevard
Golden, Colorado 80401-3393

13. Type of Report & Period Covered
Technical Report

14. 10/1/88 - 11/30/89

15. Supplementary Notes
SERI Technical Monitor: W. Luft, (303) 231-1823

16. Abstract (Limit: 200 words)

Textured tin oxide films with high light-trapping efficiency, high electrical conductivity and high transparency were successfully grown at high rates by chemical vapor deposition. This process has achieved large-scale commercial production of substrates for amorphous silicon solar cells. Highly transparent and highly conductive films of flourine-doped zinc oxide were formed by a new CVD process. Increases in the texture (light-trapping) and growth rate are needed to make this a practical process for making substrates for solar cells. Decreases in deposition temperature are needed to made successful back contacts. A hybrid TCO consisting of textured tin oxide covered with a thin, smooth flourine-doped zinc oxide layer combines the best features of these two materials. It shows efficient light-trapping because of the textured tin oxide, combined with the good resistance of zinc oxide to the hydrogen plasma used to deposit the amorphous silicon. Highly conductive and reflective titanium nitride was deposited under conditions mild enough to form back contacts on amorphous silicon solar cells. Actual cells will be coated and tested in the next contract period. Further optimization of the deposition conditions for these materials should be carried out in collaboration with solar cell manufacturers.

17. Document Analysis
a. Descriptors
Photovoltaics ; conducting materials ; thin-films ; deposition

b. Identifiers/Open-Ended Terms

c. UC Categories 270

18. Availability Statement
National Technical Information Service
U.S. Department of Commerce
5285 Port Royal Road
Springfield, Virginia 22161

19. No. of Pages
65

20. Price
A04

Form No. 0069 (3-25-82)